UNIVERSITY OF LEEDS

This is a repository copy of *Analysis of the kinetics and yields of OH radical production from the CH_3OCH_2 + O_2 reaction in the temperature range 195-650 K: an experimental and computational study*.

White Rose Research Online URL for this paper:
http://eprints.whiterose.ac.uk/101199/

Version: Accepted Version

Article:

Eskola, AJ, Carr, SA, Shannon, RJ et al. (5 more authors) (2014) Analysis of the kinetics and yields of OH radical production from the CH_3OCH_2 + O_2 reaction in the temperature range 195-650 K: an experimental and computational study. Journal of Physical Chemistry A, 118 (34). pp. 6773-6788. ISSN 1089-5639

https://doi.org/10.1021/jp505422e

(c) 2014, American Chemical Society. This document is the Accepted Manuscript version of a Published Work that appeared in final form in the Journal of Physical Chemistry A, copyright (c) American Chemical Society after peer review and technical editing by the publisher. To access the final edited and published work see https://doi.org/10.1021/jp505422e

Reuse
Unless indicated otherwise, fulltext items are protected by copyright with all rights reserved. The copyright exception in section 29 of the Copyright, Designs and Patents Act 1988 allows the making of a single copy solely for the purpose of non-commercial research or private study within the limits of fair dealing. The publisher or other rights-holder may allow further reproduction and re-use of this version - refer to the White Rose Research Online record for this item. Where records identify the publisher as the copyright holder, users can verify any specific terms of use on the publisher's website.

Takedown
If you consider content in White Rose Research Online to be in breach of UK law, please notify us by emailing eprints@whiterose.ac.uk including the URL of the record and the reason for the withdrawal request.

White Rose
university consortium
Universities of Leeds, Sheffield & York

eprints@whiterose.ac.uk
https://eprints.whiterose.ac.uk/

Analysis of the Kinetics and Yields of OH Radical Production from the $CH_3OCH_2 + O_2$ Reaction in the Temperature Range 195 – 650 K: an Experimental and Computational study

A.J. Eskola[†], S.A. Carr, R.J. Shannon, B. Wang[‡], M.A. Blitz, M.J. Pilling, P.W. Seakins*

School of Chemistry, University of Leeds, Leeds, LS2 9JT, UK

S.H. Robertson

Accelrys Ltd, Science Park, Cambridge, CB4 0WN, UK

†Current address: Combustion Research Facility, Mail Stop 9055, Sandia National Laboratories, CA 94551-0969, USA

‡Current address: College of Chemistry and Molecular Sciences, Wuhan University, Wuhan, 430072, People's Republic of China

* To whom correspondence should be addressed: email: P.W.Seakins@leeds.ac.uk, Tel +44 (0)113 3436568

Abstract

The methoxymethyl radical, CH_3OCH_2, is an important intermediate in the low temperature combustion of dimethyl ether. The kinetics and yields of OH from the reaction of the methoxymethyl radical with O_2 have been measured over the temperature and pressure ranges of 195 – 650 K and 5 – 500 Torr by detecting the hydroxyl radical using laser induced fluorescence following the excimer laser photolysis (248 nm) of CH_3OCH_2Br. The reaction proceeds via the formation of an energised $CH_3OCH_2O_2$ adduct, which either dissociates to OH + 2 H_2CO or is collisionally stabilised by the buffer gas. At temperatures above 550 K, a secondary source of OH was observed consistent with thermal decomposition of stabilized $CH_3OCH_2O_2$ radicals. In order to quantify OH production from the $CH_3OCH_2 + O_2$ reaction, extensive relative and absolute OH yield measurements were performed over the same (T, P) conditions as the kinetic experiments. The reaction was studied at sufficiently low radical concentrations ($\sim10^{11}$ cm^{-3}) that secondary (radical + radical) reactions were unimportant and the rate coefficients could be extracted from simple bi- or tri-exponential analysis. *Ab initio* (CBS-GB3) / master equation calculations (using the program MESMER) of the $CH_3OCH_2 + O_2$ system were also performed to better understand this combustion-related reaction as well as be able to extrapolate experimental results to higher temperatures and pressures. To obtain agreement with experimental results (both kinetics and yield data), energies of the key transition states were substantially reduced (by 20 – 40 kJ mol^{-1}) from their *ab initio* values and the effect of hindered rotations in the CH_3OCH_2 and CH_3OCH_2OO intermediates were taken into account. The optimised master equation model was used to generate a set of pressure and temperature dependent rate coefficients for the component nine phenomenological reactions that describe the $CH_3OCH_2 + O_2$ system, including four well-skipping reactions. The rate coefficients were fitted to Chebyshev polynomials over the temperature and density ranges 200 to 1000 K and 1×10^{17} to 1×10^{23} molecule cm^{-3} respectively for both an N_2 and He bath gas. Comparisons with an existing autoignition mechanism show that the well-skipping reactions are important at a pressure of 1 bar but are not significant at 10 bar. The main differences derive from the calculated rate coefficient for the $CH_3OCH_2OO \rightarrow CH_2OCH_2OOH$ reaction, which leads to a faster rate of formation of $O_2CH_2OCH_2OOH$.

Keywords: Dimethyl Ether Combustion, Well-Skipping, Methoxymethyl Radicals, OH Yields, Master Equation Calculations.

1. Introduction

Dimethyl ether (DME), CH_3OCH_3, is easily liquefied and can be produced from a variety of feed-stocks such as natural gas, crude oil, coal, and bio-mass.[1,2] China, having abundant coal resources, but minor oil and natural gas reserves, has strong interest in coal gasification to produce transportation fuels and production of DME is considered as an efficient end-product.[3,4] DME is a very promising alternative diesel fuel or fuel additive[5] due to its high cetane number (>55), resulting in a low auto-ignition temperature and fast vaporization. Unlike conventional diesel fuel, DME creates little or no soot when combusted at relatively low temperatures, due to the absence of carbon – carbon bonds in its molecular structure. While DME use clearly reduces sooting in compression-ignition engines, controversies exist with respect to its capability to reduce NO_x, hydrocarbon, and CO emissions as well.[6,7]

Detailed chemical kinetic models of DME autoignition, pyrolysis, and oxidation under varying temperature / pressure / equivalence ratio / residence time conditions have been developed and tested against data from several experimental systems, including jet stirred reactors,[8-10] rapid compression machine[11], variable-pressure flow reactors,[12-16] shock-tubes[17-19] and direct sampling from flames.[20,21] Despite considerable experimental and modelling effort there is still a significant lack of understanding[22] of rates, products, and mechanisms of several important reactions, particularly reactions of the methoxymethyl radical (CH_3OCH_2).

The methoxymethyl radical plays an important role both in combustion and in the atmospheric degradation of dimethyl ether. The main source of the CH_3OCH_2 radical under low temperature combustion conditions and in the Earth's atmosphere is the reaction of the OH radical with DME:[23-25]

$$OH + CH_3OCH_3 \rightarrow H_2O + CH_3OCH_2 \qquad \text{(R1)}$$

This reaction is followed, in both low temperature combustion and atmospheric chemistry, by reaction with O_2. However, in addition to the simple pressure dependent addition of O_2 and the formation of a relatively stable RO_2 peroxy radical, an additional pathway is open to the newly formed, energised peroxy radical $CH_3OCH_2O_2$*, see Scheme 1. In competition with stabilisation of $CH_3OCH_2O_2$* to $CH_3OCH_2O_2$, R2a, and re-dissociation to reactants, formation of OH + 2 H_2CO, R2b, can occur via $CH_2OCH_2OOH^*$, following an internal H abstraction and decomposition of the resultant QOOH species, CH_2OCH_2OOH.

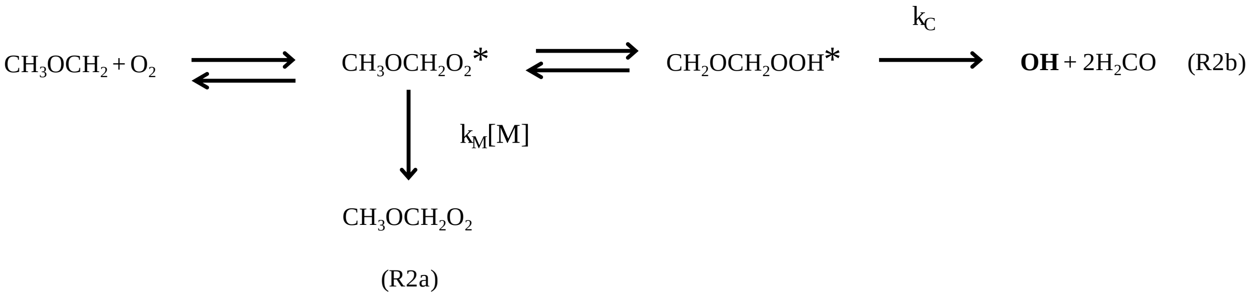

Scheme 1.

Several experimental kinetic studies of reaction 2 have been performed. At low pressures (0.6 – 6 Torr of N_2, 298 K) Masaki et al.[26] and (0.8 – 4 Torr of He, 302 – 473 K) Hoyermann et al.[27], both employed mass-spectrometry for CH_3OCH_2 radical detection. Using a UV-absorption method, Sehested et al.[28] studied the kinetics of reaction (R2) over wide pressure range (20 – 14000 Torr of SF_6) at 296 K and as a function of temperature (296 – 473 K) at 14000 Torr (18 bar). Also employing a UV-absorption method, Maricq et al.[29] measured the kinetics of reaction 2 over the pressure range (5.4 – 690 Torr of N_2) at 295 K and studied the temperature dependence of the reaction at about 120 Torr pressure in the temperature range 220 – 355 K. In previous investigations of the CH_3OCH_2 + O_2 reaction, methoxymethyl radicals were generated via the fast reaction between DME and chlorine or fluorine atoms, (k(Cl/F + DME) ≈ (1.5 − 2) × 10^{-10} cm^3 s^{-1}). However, relatively high DME concentrations were needed and so formation of OH radicals via reaction 2b complicated data interpretation because CH_3OCH_2 radicals are reformed in reaction 1, even though Cl + DME and F + DME are much faster than R1: k(Cl/F + DME) / k(OH + DME) ≈ 60 at 295 K. Another important problem, associated with the use of high DME concentrations to achieve fast CH_3OCH_2 radical formation for kinetic analysis, stems from the fact that DME undergoes thermal degradation in the presence of O_2 at temperatures above ~500 K, as has been observed by Rosado-Reyes et al.[30] Recently, in this laboratory, Eskola et al.[31] measured the kinetics and yields of OH radical at 295

K from reaction 2 using a direct photolytic source of the CH_3OCH_2 radical, CH_3OCH_2Br, for the first time.

There are some computational studies of reaction 2. Yamada et al.[32] performed CBS-q and G2 composite *ab initio* calculations with a QRRK analysis to calculate energy-dependent rate constants, which were employed in master equation simulations to account for collisional stabilization of intermediate species. In order to fit the experimental H_2CO yield of reaction 2 at 296 K in the pressure range 0.38 – 940 Torr, measured by Sehested et al.[33], Yamada et al. reduced the energy of the transition state for CH_2OCH_2OOH decomposition (TS2, highest energy transition state between reactants and OH + $2H_2CO$ products) by about 20 kJ mol^{-1}, which is large compared to the typical uncertainties of such calculations. Subsequently Anderson and Carter[34] performed UDFT/6-31G** and UDFT/6-311G** calculations for reaction 2 and obtained energies of the potential energy surface that were significantly different from those of Yamada et al.[32]

In this article the kinetics of the $CH_3OCH_2 + O_2$ reaction has been investigated as a function of pressure (5 – 500 Torr) over the temperature range 195 – 650 K by monitoring hydroxyl radical formation using laser induced fluorescence (LIF). Relative determinations of OH yields from reaction 2 were performed, as a function of pressure and temperature, using several CH_3OCH_2 radical sources and employing a Stern Volmer analysis.[31] The results from the Stern Volmer analysis are compared with those from absolute yield / recycling measurements of the OH radical from reactions 1 and 2, which were also performed over comparable pressure and temperature ranges. In addition, CBS-GB3 composite *ab initio* calculations of reaction 2 have been performed to obtain energetics, vibrational frequencies, and moments of inertia for intermediates, transition states, and stable species. Internal rotation barrier heights and moments of inertia of certain intermediates have also been calculated. This information was subsequently used in master equation simulations, which were performed using the MESMER-program.[35] The effect of treating certain lowest-frequency vibrations as internal rotations (hindered internal rotation model) instead of considering all calculated frequencies as vibrations (vibration-only-model) is also investigated in the current work.

2. Experimental

The apparatus, which uses conventional slow flow laser flash photolysis combined with LIF detection of OH, has been described previously.[24,31,36-39] The CH_3OCH_2 or OH radical precursor(s), reactant (O_2), and buffer gas (He or N_2) were premixed in a mixing manifold before being flowed through the reaction cell. Two different reaction cells, both made of stainless steel, were used for sub-ambient and for high-temperatures. For sub-ambient temperature studies, the cell was cooled by an *i*-propylalcohol/dry-ice – mixture down to 195 K, whereas for high-temperature experiments, the cell was heated by cartridge heaters. In both cases, the temperature was measured using a K-type thermocouple in the central portion of the cell. Gases were flowed through calibrated mass flow controllers and the pressure in the cell was measured using capacitance manometers and adjusted by throttling the exit valve on the cell.

In the current work two methods were employed to produce methoxymethyl and hydroxyl radicals. Photolysis of CH_3OCH_2Br at 248 nm has been shown to be convenient direct source of CH_3OCH_2 radical and it was used in all kinetic and some OH-yield studies of reaction 2.[31]

$$CH_3OCH_2Br + h\nu\ (\lambda = 248\ \text{nm}) \rightarrow CH_3OCH_2 + Br \qquad \text{(P1a)}$$

$$\rightarrow \text{other products} \qquad \text{(P1b)}$$

Alternatively methoxymethyl radicals were produced indirectly via photolysis of oxalyl chloride[40] and subsequent fast chlorine atom reaction with DME.[41] The chlorine atom yield from 248 nm photolysis is uncertain, especially at low pressures and temperatures.[40]

$$(COCl)_2 + h\nu\ (\lambda = 248\ \text{nm}) \rightarrow CO + Cl + COCl\ /\ CO + Cl \qquad \text{(P2)}$$

$$(COCl)_2 + h\nu\ (\lambda = 193\ \text{nm}) \rightarrow 2\ CO + 2\ Cl \qquad \text{(P3)}$$

$Cl + CH_3OCH_3 \rightarrow CH_3OCH_2 + HCl$ (R3)

$Cl \rightarrow$ loss (R4)

Several methods to produce OH radicals were also employed. Excimer laser photolysis of *t*-C_4H_9OOH (or formic acid) at 248 nm was used to produce OH directly.

t-$C_4H_9OOH + h\nu\ (\lambda = 248\ \text{nm}) \rightarrow$ *t*-$C_4H_9O + OH$ (P4a)

$\rightarrow$ other products (P4b)

At 195 K no peroxides or acids can be used due to their low vapour pressure and other methods to produce OH radicals had to be invoked. In the absence of molecular oxygen and using helium buffer gas, photolysis of N_2O at 193 nm and the subsequent fast reaction of $O(^1D)$ with DME was employed.

$N_2O + h\nu\ (\lambda = 193\ \text{nm}) \rightarrow O(^1D) + N_2$ (P5)

$O(^1D) + CH_3OCH_3 \rightarrow OH +$ products (R5)

$O(^1D) \rightarrow$ loss (R6)

The presence of O_2 in high concentrations in recycling measurements precludes the above method for the production of OH due to rapid quenching of $O(^1D)$ by oxygen. However, Carr et al.[37] have shown that photolysis of acetone at 248 nm in the presence of O_2 is a potential source of OH:

$CH_3COCH_3 + h\nu\ (\lambda = 248\ \text{nm}) \rightarrow CH_3CO + CH_3$ (P6a)

$\rightarrow$ other products (P6b)

$CH_3CO + O_2 \rightarrow OH +$ products (R7a)

$CH_3CO + O_2 + M \rightarrow CH_3CO(O)_2 + M$ (R7b)

The photolytic precursors, CH_3OCH_2Br, $(COCl)_2$, *t*-C_4H_9OOH, HCOOH and CH_3COCH_3 were photolysed using an excimer laser operating at 248 nm (KrF, Lambda Physik, Compex) with a photon density typically between 1 and 7 × 10^{16} photon cm^{-2}. The same laser, but operating at 193 nm (ArF), was used to photolyse N_2O, but with a much lower photon density, typically about 6 × 10^{13} photon cm^{-2}, in order to avoid photolysis of DME. Typical radical concentrations, for all methods of generation were 10^{11} molecule cm^{-3}.

OH radicals were probed using off-resonance laser induced fluorescence. Probe light at ~281.9 nm, corresponding to the energy of the OH ($A^2\Sigma(v = 1) \leftarrow X^2\Pi(v = 0), Q_1(1)$) transition, was obtained from the frequency doubled output of a dye laser (Spectra-Physics, Quanta-Ray, PDL-3, Rhodamine 6G dye), which was pumped at 532 nm by an Nd:YAG laser (Spectra Physics, Quanta-Ray, QCR 100-series). Off-resonance fluorescence at ~308 nm was collected by a quartz lens and passed through an interference filter (Barr Associates Inc., 308.5 ± 5 nm) before it was detected using a photomultiplier (EMI 9813). The signal from the photomultiplier was integrated with a boxcar averager, whose output was digitised and passed to a personal computer for subsequent data analysis. The delay time between the photolysis laser and probe laser was scanned using a delay generator such that the recorded OH temporal profile typically consisted of 500 time points, each averaged over 3 – 5 laser shots. The pulse repetition frequency of the lasers was varied between 10 and 5 Hz, and the total flow rate of gas ensured there was a fresh sample for each laser shot. The typical initial concentration of radicals in the system was estimated to be about 1 × 10^{11} cm^{-3}.

Radical precursors, CH_3OCH_2Br (bromomethoxymethane) (tech. 90 %), CH_3OCH_3 (dimethyl ether) (99 %), $(COCl)_2$ (oxalyl chloride, >99%), CH_3COCH_3 (acetone) and *t*-C_4H_9OOH (*t*-butyl hydroperoxide, 70 % aqueous solution), supplied by Aldrich, were degassed and diluted in He. O_2 (Air Products, high purity, 99.999%) gas was either diluted in He or used straight from the cylinder. Helium (BOC, CP grade, 99.999%), N_2 (BOC, UHP grade), and N_2O (BOC, 99.9%) were used straight from the cylinder.

3. Experimental results

3.1 Kinetics of $CH_3OCH_2 + O_2$ reaction

The rate coefficients for reaction 2, as a function of temperature and pressure, were obtained using bromomethoxymethane as the photolytic precursor. When CH_3OCH_2Br was photolysed at 248 nm in the presence of added O_2 in the reaction mixture, OH formation was observed; a typical kinetic trace is shown in the inset of Figure 1. This behaviour is qualitatively consistent with OH formation as a primary product of a reaction involving O_2.[33] No direct photolytic hydroxyl radical formation was observed. OH is formed in reaction 2, and the subsequent slow loss of OH from the system, reaction 8, is due to the reaction with CH_3OCH_2Br and diffusion out of the measuring volume, which depends on the total pressure.

$$\mathrm{OH} \rightarrow \mathrm{loss} \tag{R8}$$

The solution for the kinetics of OH formed in reaction 2b and reacting subsequently by reaction 8 gives the following biexponential equation, E1:

$$[\mathrm{OH}] = \frac{\{\alpha[\mathrm{CH_3OCH_2}]_0\}\mathrm{k}_2'}{\mathrm{k}_2' - \mathrm{k}_8'}\left[\exp\left(-\mathrm{k}_8' t\right) - \exp\left(-(\mathrm{k}_2' + \mathrm{k}_i)t\right)\right] \tag{E1}$$

where $\alpha = \mathrm{k}_{2b}/\mathrm{k}_2$, $[\mathrm{CH_3OCH_2}]_0$ = initial methoxymethyl radical concentration, $\mathrm{k}_2' = \mathrm{k}_2[\mathrm{O_2}]$, the pseudo first-order rate coefficient for reaction 2, obtained under conditions where $[O_2] \gg [CH_3OCH_2]_0$ and k_8' is the first-order rate coefficient for loss of OH by reaction 8. The parameters of equation (E1) were fitted to the experimental data using a non-linear least-squares method, treating k_2', k_8', and the relative values of $\{\alpha[\mathrm{CH_3OCH_2}]_0\}$, as variable parameters. The returned values of k_8' were typically in the range 1000 – 3500 s^{-1} and $[O_2]$ was always high enough so that $\mathrm{k}_2' \gg \mathrm{k}_8'$. The bimolecular reaction rate coefficient k_2 was derived from the slope of the plot of $\mathrm{k}_2' + k_i$ versus $[O_2]$ An example of such a plot is shown in Figure

1; a good linear relationship was observed for all bimolecular plots, with an intercept corresponding to k_i due to other methyoxymethyl loss processes [31] (equation E1).

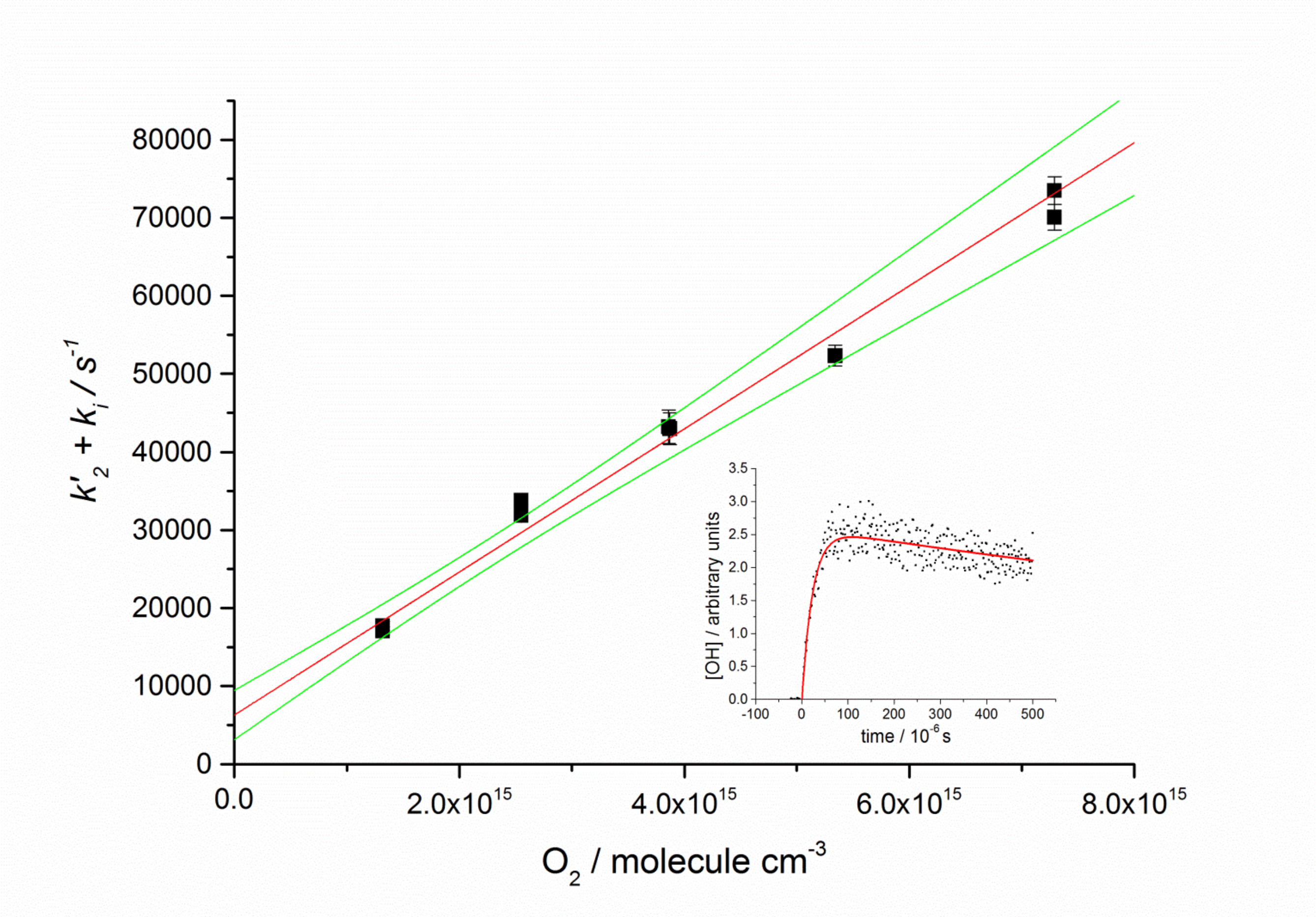

Figure 1. Plot of the first order CH_3OCH_2 decay rate coefficient k'_2 versus $[O_2]$ 250 Torr He. Linear least-square fit of the data and the corresponding upper and lower 95 % confidence limits are also shown. The inset shows a kinetic trace for OH formation from the $CH_3OCH_2 + O_2$ reaction 2 at 250 Torr He, and $[O_2] = 6.48\times10^{15}$ molecule cm^{-3}. The solid line represents a fit to the data using equation 1, returning $k'_2 = (42970 \pm 2030)$ s^{-1} where the error is statistical at the 1σ level.

The bimolecular rate coefficients for reaction 2 at various temperatures, buffer gas densities (0.11 – 12.5)×10^{18} cm^{-3}, and corresponding experimental conditions are given in Table S1 of the Supplementary Information.

Above 500 K the kinetic traces became more complex as illustrated in Figure 2. A fast production of OH via reaction 2b was still observed, consistent with that at lower temperatures, but rather than the OH signal reaching a maximum and slowly decaying due to diffusive or other first order loss processes (inset to Figure 1), the OH signal continued to grow more slowly on a ms timescale as illustrated in Figure 2. At 550 K and above, the OH profiles were analysed by fitting to a triexponential equation incorporating both the primary and secondary OH production and OH loss by reaction 8:

$$[\mathrm{OH}(t)] = D\exp(\lambda_{e1}t) + E\exp(\lambda_{e2}t) + F\exp(-k_8t) \tag{E2}$$

where D, E and F are constants and the experimental eigenvalues λ_{e1} and λ_{e2} correspond to the reciprocal time coefficients for secondary and primary OH production respectively. The full scheme of phenomenological reactions for the $CH_3OCH_2 + O_2$ system comprises:

$CH_3OCH_2 + O_2 \rightarrow RO_2\ (CH_3OCH_2O_2)$ (R2a)

$CH_3OCH_2 + O_2 \rightarrow OH + 2CH_2O$ (R2b)

$CH_3OCH_2 + O_2 \rightarrow QOOH\ (CH_2OCH_2OOH)$ (R2c)

$RO_2 \rightarrow CH_3OCH_2 + O_2$ (R9a)

$RO_2 \rightarrow OH + 2CH_2O$ (R9b)

$RO_2 \rightarrow QOOH$ (R9c)

$QOOH \rightarrow CH_3OCH_2 + O_2$ (R10a)

$QOOH \rightarrow OH + 2CH_2O$ (R10b)

$QOOH \rightarrow RO_2$ (R10c)

and the potential energy surface for the reaction is shown in more detail in Figure 8 in section 4.1. Using the above scheme, a steady state analysis can be performed in order to equate the eigenvalues, λ_{e1} and λ_{e2} from the tri-exponential analysis with combinations of the phenomenological rate coefficients and this analysis is presented in the supplementary information. Master equation calculations have also been performed, which are described in section 4.2, and to complement the analysis in the supplementary information, the calculated eigenvalues and phenomenological rate coefficients are shown as a function of temperature in Figures S2 and S3 of the supplementary information. Assuming the chemistry is described entirely by the above scheme, the experimental eigenvalues λ_{e1} and λ_{e2} are equivalent to the theoretical eigenvalues λ_1 and λ_2 after suitable correction for the intercept in Figure 2.From the master equations calculation, under all experimentally relevant conditions, it is found that the modulus of the eigenvalue λ_2 can be equated with the total loss rate coefficient for CH_3OCH_2 (k_2). In the 550 - 650 K window, the largest contribution to λ_1 is from the well skipping thermal decomposition of RO_2 ($CH_3OCH_2O_2$) to form OH (k_{9b}). Isomerisation of RO_2 to QOOH (k_{9c}), followed by dissociation to form OH (k_{10b}) is less important because QOOH rapidly isomerises back to RO_2 so that its steady state concentration is low. There is a small contribution to secondary OH formation via re-dissociation of RO_2 back to reactants followed by the well skipping reaction R + O_2 to form OH (k_{9a}, k_{2b}).

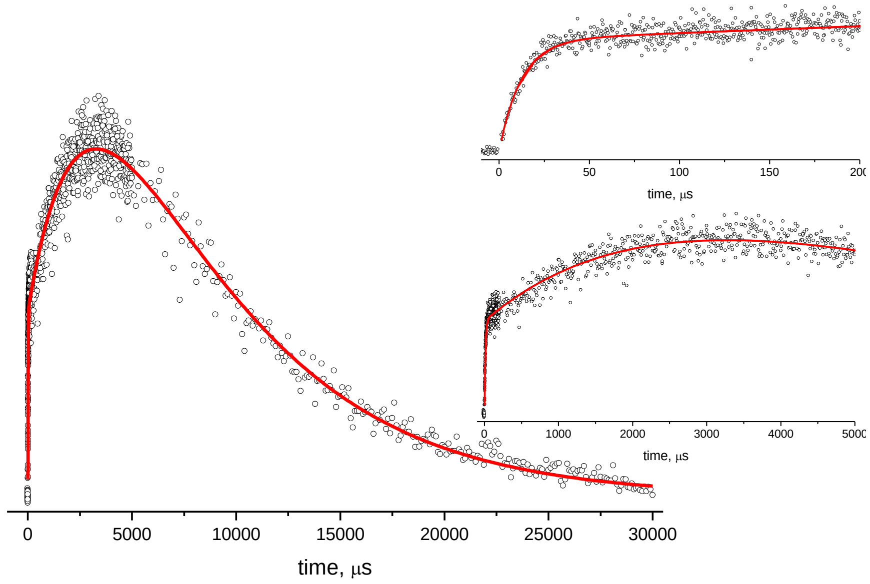

Figure 2. The main figure shows the tri-exponential OH profile at 550 K and 500 Torr of He. The upper inset at short time shows that, at this temperature, the primary and secondary growth can readily be separated; the lower inset shows the same but over longer time.

However there is an alternative explanation for the secondary OH production due to the possibility of interception of the QOOH species by O_2. The bimolecular reaction between QOOH and O_2 can potentially form two OH radicals leading to chain branching and, if QOOH is sufficiently long lived under our experimental conditions, then the secondary OH formation observed could be attributed to OH production via the QOOH + O_2 reaction. The origins of the long-time OH production are discussed in more detail in Section 6 with the aid of master equation calculations and numerical integration.

At higher temperatures, λ_{e1} was obtained more precisely by working at longer timescales, treating the primary production as essentially a prompt OH source, and analysing the secondary production and OH loss as a bi-exponential process, with an equation similar to E1. The data for the temperature dependence of λ_{e1} are tabulated in Table S2.

The results of the kinetics studies of the primary OH production are shown in Figure 3. A detailed comparison of the room temperature measurements with the previous literature can be found in our previous publication.[31]

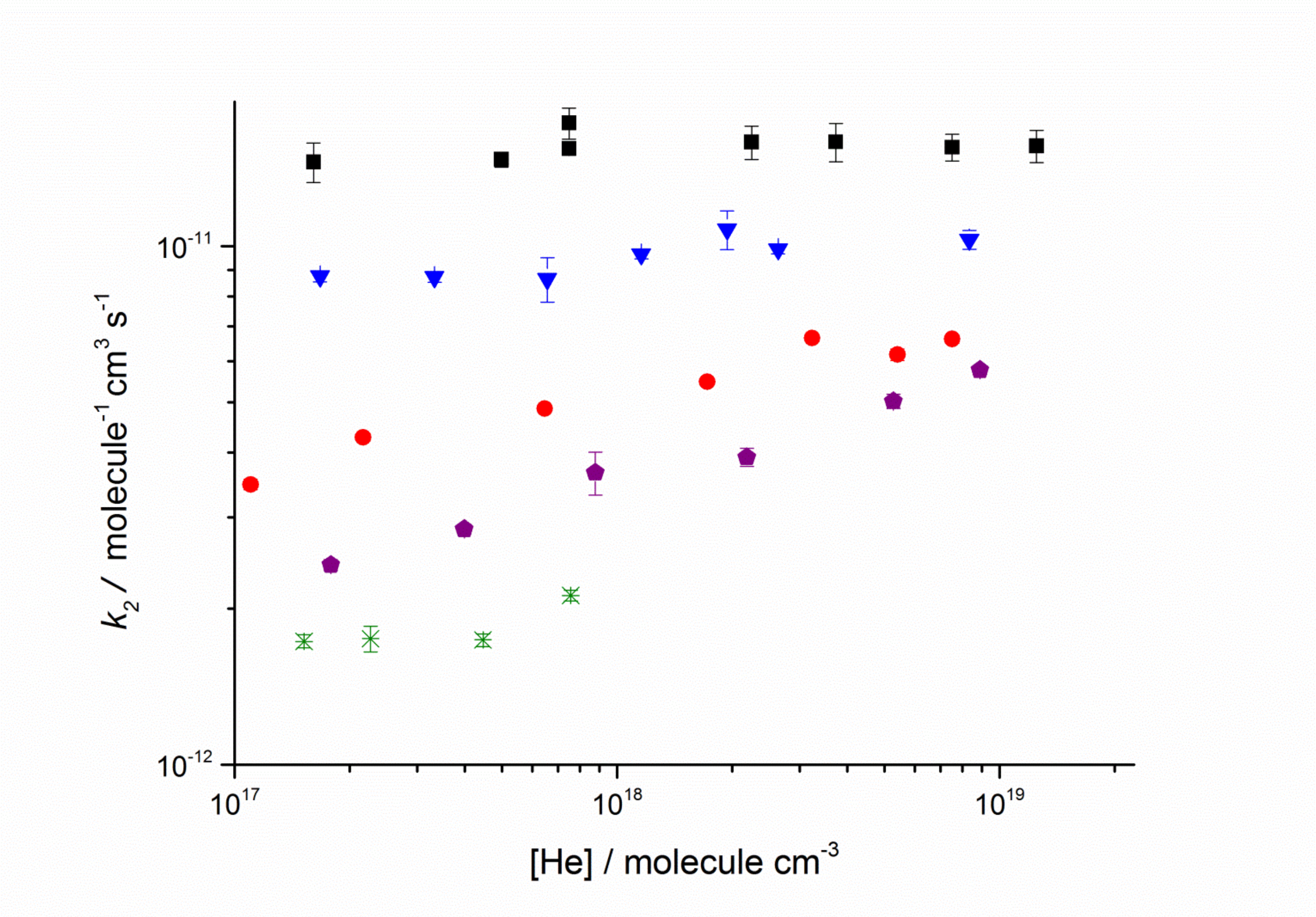

Figure 3. Plots of the bimolecular rate coefficients for the $CH_3OCH_2 + O_2$ reaction (R2) versus buffer gas density. Black squares correspond to data at 195 K, blue triangles to 296 K, red circles to 450 K, purple hexagons to 550 K and green stars corresponds to 650 K. Both rate coefficient and bath gas density are plotted on logarithmic scales.

Apart from 298 K, there are no previous pressure dependent studies with which to compare our current temperature and pressure dependent data. The 295 K data measured in helium, obtained as part of a previous publication,[31] but using the same apparatus and methods as this work, are not directly comparable with the previous literature which used N_2[29] and SF_6[28] as a bath gas. Our rate coefficients at 295 K in helium are approximately 10 – 30% higher than the previous literature values (see Figure 2 of Eskola et al.[31]). Somewhat surprisingly, experiments in N_2 and SF_6 appear to lie on a common line.

3.2 Relative determination of OH yield

OH yield measurements, together with the rate coefficient determinations for reactions (R2) and (R9) discussed above, provide essential information for the overall characterisation of the $CH_3OCH_2 + O_2$ reaction system and the master equation analysis and fitting described below. This section discusses OH yield measurements using a relative technique and section 3.3 discusses an absolute method. The results are analysed using a simple Lindemann approach in order to convert the relative yields into absolute yields and to facilitate comparisons with results from other laboratories.

3.2.1 *CH_3OCH_2Br photolysis*

As is shown in Scheme 1, the excited peroxy radical ($CH_3OCH_2O_2$*) can either be collisionally stabilized or, alternatively, an internal abstraction can take place with subsequent dissociation producing OH, with the fraction of the latter process decreasing with the total gas density [M]. Back-to-back experiments at reference and test pressures, were performed to measure the relative OH yield as a function of gas density at 195, 450, 550 and 650 K using the CH_3OCH_2Br radical precursor.[31] The concentrations of O_2 and bromomethoxymethane (and thus $[CH_3OCH_2]_0$) were held constant as the total helium gas density was varied. The parameters in equation 1 were fitted to the data from these experiments to obtain relative values of $\{\alpha[\mathrm{CH_3OCH_2}]_0\}$ over a range of helium total gas densities.

A simple Lindemann analysis of Scheme 1 gives $\alpha = \mathrm{k_C}/(\mathrm{k_C} + \mathrm{k_M}[\mathrm{He}])$ with $\alpha = 1$ at [He] = 0. This analysis assumes that there are no additional bimolecular product channels that do not produce OH and that helium does not quench OH fluorescence.

The relative yield, β, is defined as:

$$\beta = \frac{\{\alpha[\mathrm{CH_3OCH_2}]_0\}}{\{\alpha_{\mathrm{ref}}[\mathrm{CH_3OCH_2}]_0\}} = \frac{\alpha}{\alpha_{\mathrm{ref}}} = \frac{1+(\mathrm{k_{He}}/\mathrm{k_C})[\mathrm{He}]_{\mathrm{ref}}}{1+(\mathrm{k_{He}}/\mathrm{k_C})[\mathrm{He}]} \tag{E3}$$

where α_{ref} is the OH yield at the reference gas density, $[\mathrm{He}]_{\mathrm{ref}}$, and $\{\alpha_{\mathrm{ref}}[\mathrm{CH_3OCH_2}]_0\}$ is the corresponding value, multiplied by $[\mathrm{CH_3OCH_2}]_0$, returned by fitting equation (E1) to the data. k_{He} is the stabilising rate coefficient for helium. For equation 3 to be valid, $[\mathrm{CH_3OCH_2}]_0$ has to be independent of pressure. Then

$$\frac{1}{\beta} = \alpha_{\mathrm{ref}}\,(1+\frac{\mathrm{k_{He}}}{\mathrm{k_C}}[\mathrm{He}]) \tag{E4}$$

A plot $1/\beta$ vs. [He] is a straight line, with the slope/intercept ratio = $\mathrm{k_{He}}/\mathrm{k_c}$, which allows $\alpha_{\mathrm{ref}} = 1/(1+(\mathrm{k_{He}}/\mathrm{k_C})[\mathrm{He}]_{\mathrm{ref}})$ to be determined and hence α to be determined at all pressures, by rescaling the relative yields β to absolute yields using $\alpha = \beta\alpha_{\mathrm{ref}}$. Note that these values are based on the assumption that $\alpha = 1$ at [He] = 0. In designing the experiments, the most accurate rescaling of β is achieved by making $[\mathrm{He}]_{\mathrm{ref}}$ close to zero, so that uncertainties resulting from the determination of $\mathrm{k_{He}}/\mathrm{k_C}$ are minimised.

For example, fitting equation 4 to the weighted data obtained at 195 K with $[\mathrm{He}]_{\mathrm{ref}}(195\ \mathrm{K}) = 7.52 \times 10^{17}$ molecule cm^{-3} gives a straight line with slope/intercept ratio = $\mathrm{k_{He}}/\mathrm{k_C}\,(195\mathrm{K}) = (4.35 \pm 0.07) \times 10^{-18}$ cm^3 and $\alpha_{\mathrm{ref}}(195\ \mathrm{K}) = (0.251 \pm 0.002)$ where the uncertainties quoted refer to the 95% confidence limits and that for $\mathrm{k_{He}}/\mathrm{k_C}$ includes the propagated uncertainties derived from both the slope and the intercept. The absolute values of α obtained at 195 and 450 K by rescaling the relative yields are given in Table S3 and are shown in Figure 4.

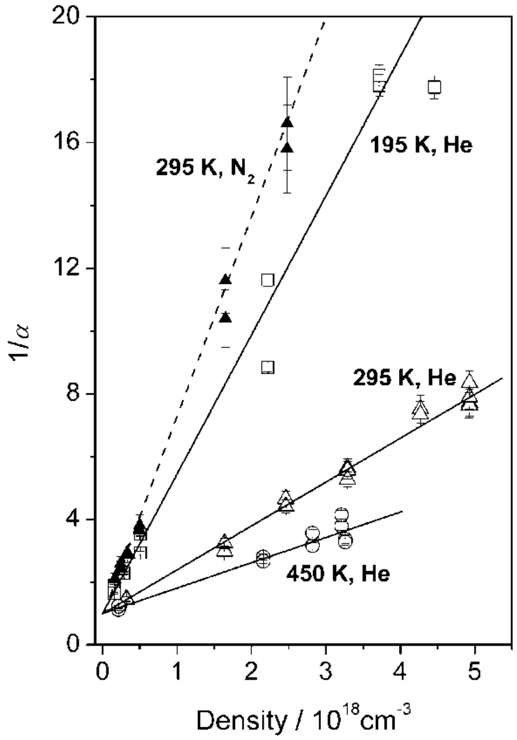

Figure 4. Inverse of the OH radical yield from CH_3OCH_2 + O_2 reaction 2 versus [He] at 195, 295, 450 K and [N_2] at 295 K. Results were obtained by the relative yield method using CH_3OCH_2Br. The gradients ($k_{|M}/k_c$) are: 195 K He; (4.35 ± 0.07) × 10^{-18} molecule cm^3, 295 K He; (1.40 ± 0.14) × 10^{-18} molecule cm^3, 450 K He; (8.06 ± 0.41) × 10^{-19} molecule cm^3, 295 K N_2; (6.05 ± 0.54) × 10^{-18} molecule cm^3. The values at 295 K, He are from our earlier work.[31]

In this work relative OH yield experiments were also performed at 298 K using N_2 buffer gas instead of helium and additional experimental considerations for these experiments are given in the supplementary information. As for the helium buffer gas studies, back-to-back experiments were performed to measure the relative OH yield as a function of [N_2] at 295 K using the CH_3OCH_2Br radical precursor. The weighted data at 295 K gives the slope/intercept; k_{N_2} / k_c = (6.05 ± 0.54) × 10^{-18} molecule cm^3 and α_{ref} = (0.191 ± 0.016) where the uncertainties quoted refer to the 95% confidence limits and that for k_{N_2}/k_C includes the propagated uncertainties derived from both the slope and the intercept. The absolute values of α obtained at 295 K in N_2 by rescaling the relative yields are given in Table 1 and are shown in Figure 4.

3.2.2 *$(COCl)_2$ photolysis in the presence of CH_3OCH_3*

In addition to the photolysis of bromomethoxymethane, oxalyl chloride photolysis at 193 or 248 nm (P2a, P3a) and subsequent reaction of Cl-atoms with DME (P2b, P3b) was used to produce CH_3OCH_2 at 298 and 450 K. The Cl + DME reaction is much faster than OH + DME, k(Cl + DME)[41] / k(OH + DME)[24] ≈ 59 and 35 at 295 and 450 K, respectively. The simple Lindemann analysis returned values of $\{\alpha[\mathrm{CH_3OCH_2}]_0\}$ from fitting equation (E1) to the data, which were used in equation 3 to calculate values of β. Plots of $\frac{1}{\beta}$ vs [He] obtained at 295 and 450 K using both 193 and 248 nm photolysis are shown in Figure 5 and $\mathrm{k_{He}/k_C}$ values from fitting equation 4 to the weighted data are given in Table 1.

3.3 Absolute determination of the OH yield; kinetics of OH + CH_3OCH_3 with and without O_2

Absolute yields of OH radicals from the $CH_3OCH_2 + O_2$ reaction (R2) were determined using recycling experiments,[42-44] which do not entail any assumption of the value of the yield of OH at zero pressure and provide an additional independent test of Scheme 1. Absolute yield experiments were performed by measuring the kinetics of the OH + CH_3OCH_3 reaction 1 in the absence and presence of O_2 at different total (He or N_2) gas densities, see Scheme 2.

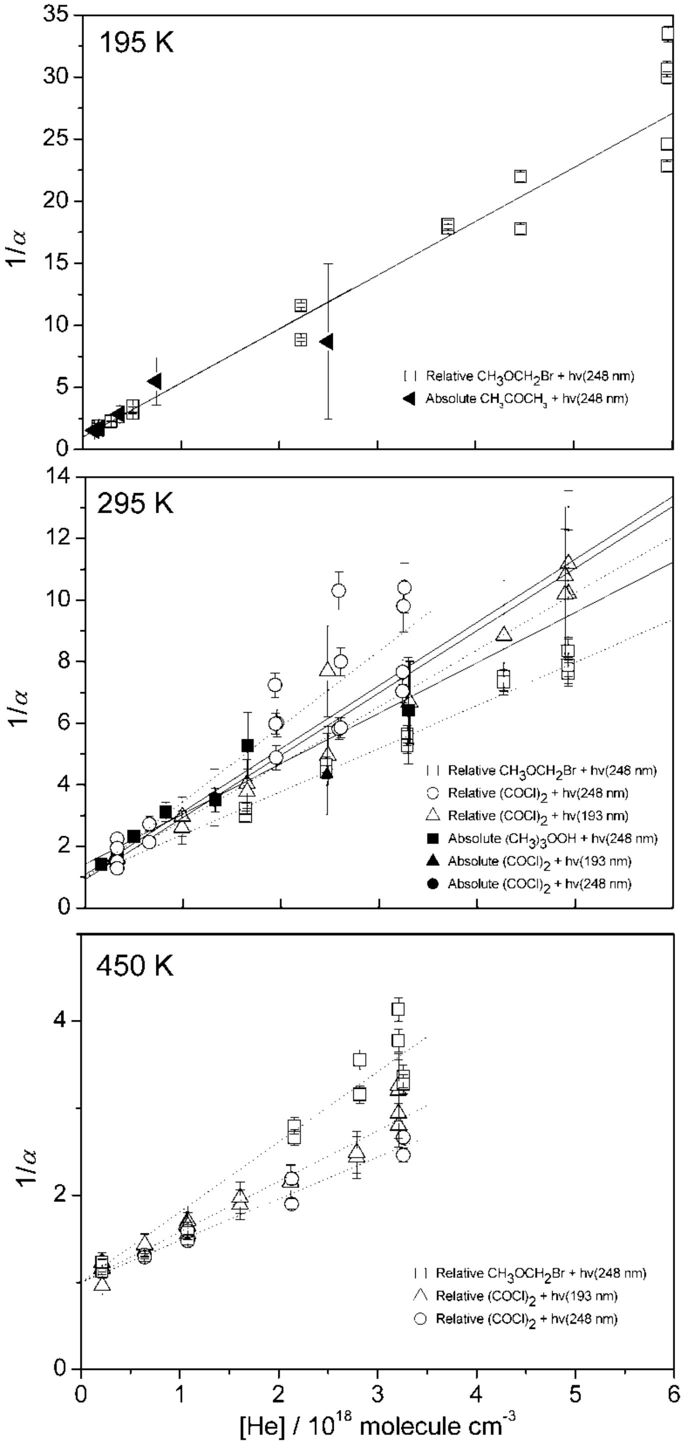

Figure 5. Comparison of Stern-Volmer plots from relative (open symbols) and absolute (filled symbols) OH radical yield measurements of $CH_3OCH_2 + O_2$ reaction 2 versus [He] at 195, 295, and 450 K. The methods of fitting these data are discussed in the text.

Table 1. Quenching coefficients, k_M/k_C (M = He, N_2), for the $CH_3OCH_2 + O_2$ reaction obtained in the current work and comparison with previous measurements from literature.[a]

Reference	Product detected	Bath Gas	Precursor	Technique[b]	T / K	P / Torr	k_M/k_C [c]
Sehested et al.[33]	CH_3OCHO + CH_3OCH_2OOH + CH_2O + CO	N_2	Cl+DME	FTIR/PS	296	0.38 − 940	3.13 ± 0.51
Maricq et al.[29]	CH_2O	N_2	Cl+DME	TIR/CM	230	4.9 – 34.7	[d]4.8
					295	4.9 – 80.3	[d]4.3
					350	5.0 – 50.0	[d]2.9
Rosado-Reyes et al.[30]	CH_2O and CH_3OCHO	N_2	Cl + DME	TIR/CM	295	10-200	[e] 7.15
					450	10-200	[e] 0.87
This work and Eskola et al.[31]	OH	He	CH_3OCH_2Br + hν (248 nm)	LIF/RM	195	3.15-153	4.35 ± 0.07
					295	9.90-151	[f]1.40 ± 0.14
					450	9.93-147	0.81 ± 0.41
This work	OH	He	Cl + DME (248 nm)	LIF/RM	295	10.1-99.3	2.5 ± 3.1
					450	30-152	0.48 ± 0.02
This work	OH	He	Cl + DME (193 nm)	LIF/RM	295	9.9-151	1.84 ± 0.36
					450	9.98-150	0.58 ± 0.07
This work	OH	N_2	CH_3OCH_2Br + hν (248 nm)	LIF/RM	295	5.3-95.3	6.05 ± 0.54
This work and Eskola et al.[31]	OH	He	OH + DME	LIF/AM	195	5.92-153	4.36 ± 1.50
					295	5.01-249	[f]2.00 ± 0.44
					450	10.02-250	0.39 ± 0.04
This work	OH	He	Cl + DME (248 nm)	LIF/AM	295	10.1-40.2	1.86 ± 0.17
					450	50.1-80.2	1.83 ± 0.17
This work	OH	He	Cl+DME (193 nm)	LIF/AM	295	10.0-75.11	2.50 ±0.95
					450	5.02-80.1	1.50 ± 0.06
This work	OH	N_2	Cl + DME (193 nm)	LIF/AM	295	5−25.01	4.71 ± 0.14
					450	5-99.98	2.36 ± 0.12

[a] Errors represent 2σ for the absolute method and the half width of the 95% confidence limits for the relative methods. [b] Explanations of used abbreviations: FTIR - Fourier transform infrared spectroscopy, PS – product study, TIR – transient infrared, CM – fit to a chemical model, LIF – laser induced fluorescence, RM – relative method, AM – absolute method. [c] Units – 10^{-18} cm^3 $molecule^{-1}$. [d] Values area lower limits. [e] Given in the reference in Arrhenius form $k_M/k_C = 1.6^{+2.4}_{-1.0} \times 10^{-20} \exp(1800 \pm 400/T)$ cm^3 $molecule^{-1}$ ($295 \leq T \leq 600$ K). [f] Reference Eskola et al.[31]

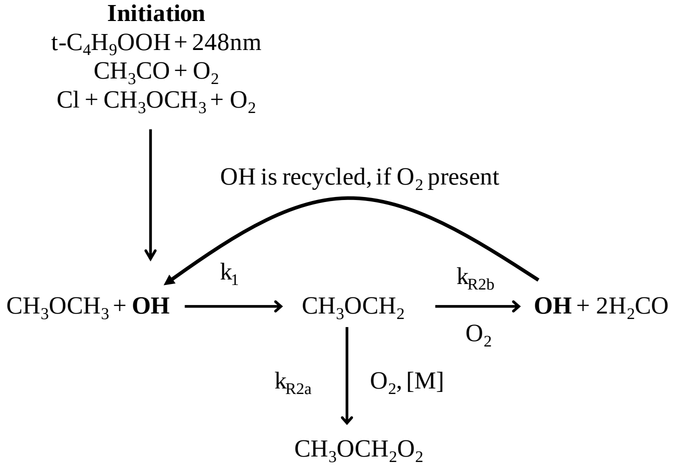

Scheme 2.

In these recycling experiments several $\mathrm{CH_3OCH_2}$ and OH radical sources were employed. Photolysis of *t*-$\mathrm{C_4H_9OOH}$ at 248 nm, (P4a), was an instant source of OH, while the other methods used, P2, P5, and P6, rely on fast chemical reactions to produce either $\mathrm{CH_3OCH_2}$ or OH or both. When $\mathrm{O_2}$ was present, its concentration was set sufficiently high that $k_7[\mathrm{O_2}]$ » $k_1[\mathrm{CH_3OCH_3}]$, $k_2[\mathrm{O_2}]$ » $k_1[\mathrm{CH_3OCH_3}]$, and $[\mathrm{CH_3OCH_3}]$ » [OH]. Under these conditions, OH regeneration via reaction 2 is rapid and the hydroxyl radical decay is a single exponential and can be described as:

$$[\mathrm{OH}]_t = [\mathrm{OH}]_0 \times \exp\left(-\left(k_1'(\pm \mathrm{O_2}) + k_8'\right)t\right), \tag{E5}$$

where $k_1' = k_1'(-\mathrm{O_2})$ means $[\mathrm{O_2}] = 0$ and $k_1'(+\mathrm{O_2})$ refer to experiments where $\mathrm{O_2}$ was present. At low [He, $\mathrm{N_2}$] the $\mathrm{O_2}$ addition has the most pronounced effect on the hydroxyl radical decay, because OH radicals are reformed efficiently via reaction 2b. Phenomenological rate coefficients were determined as:

$$k_1'(-\mathrm{O_2}) = k_1' = k_1[\mathrm{CH_3OCH_3}] \tag{E6}$$

$$k_1'(+\mathrm{O_2}) = k_1(+\mathrm{O_2})[\mathrm{CH_3OCH_3}] = k_1(1-\alpha)[\mathrm{CH_3OCH_3}] \tag{E7}$$

From equations 6 and 7 the absolute OH yield from reaction 2, α, can be obtained:

$$\alpha = \left(1 - \frac{k_1(+\mathrm{O_2})}{k_1}\right) \tag{E8}$$

Bimolecular plots of $(k_1' + k_8')$ and $(k_1'(+O_2) + k_8')$ versus [CH_3OCH_3] at different total helium pressures at 195 K are shown in Figure 6. In the absence of O_2 OH was generated via P5 and reaction 5, while in the presence of O_2 it was produced via P6 and reaction 7.[37] Recycling measurements were performed at different total helium pressures under conditions where $k_2[O_2] \gg k_1[CH_3OCH_3]$. The absolute yield measurements are given in Table S4 and the corresponding bimolecular rate coefficients as well as the values of α obtained are shown in Table S5 along with the experimental conditions.

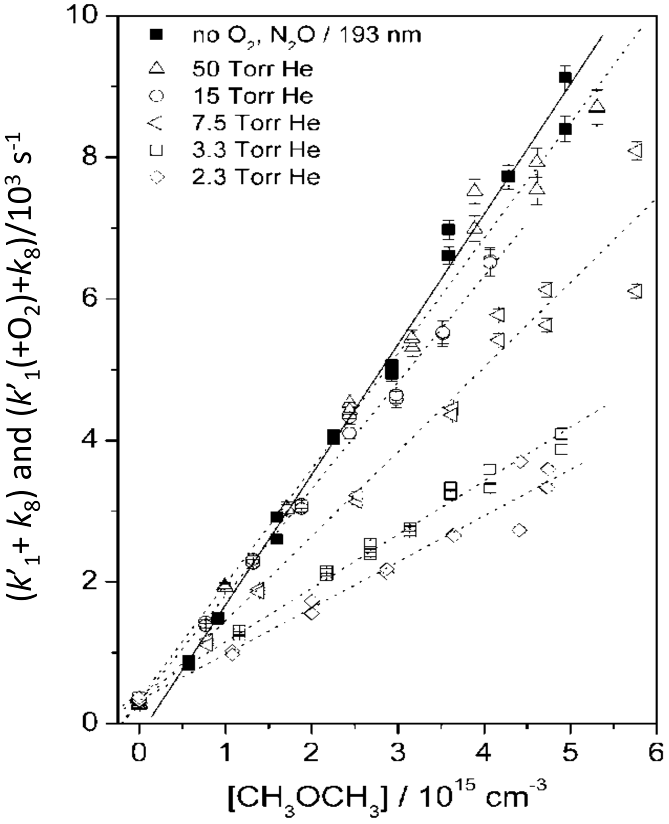

Figure 6. Bimolecular plots of OH + CH_3OCH_3 reaction (R1) in the absence (filled symbols) and presence (open symbols) of O_2 from experiments used to determine the absolute OH yield from $CH_3OCH_2 + O_2$ reaction 2 at 195 K.

Plots of $1/\alpha$ determined by the absolute and relative methods at 195, 295, and 450 K are shown in Figure 5 as a function of total helium gas density, as well as weighted linear fits of the data to the equation $1/\alpha = 1 + (k_{He}/k_C)[He]$. The slope for the values determined by the absolute method at 195 K gives k_{He}/k_C = (4.36 ± 1.50) × 10^{-18} cm^3 in good agreement with the relative method ((4.35 ± 0.07) ×

10^{-18} molecule^{-1} cm^3 with an intercept (1.03 ± 0.23). The uncertainties quoted refer to the 95% confidence limits.

The absolute method was also employed to determine OH-yields using nitrogen as buffer gas and results are shown in Figure 7. Values of k_M/k_C (M = He, N_2), quenching coefficients, obtained for the $CH_3OCH_2 + O_2$ reaction in the current work as well as comparison with previous measurements from literature are shown in Table 1.

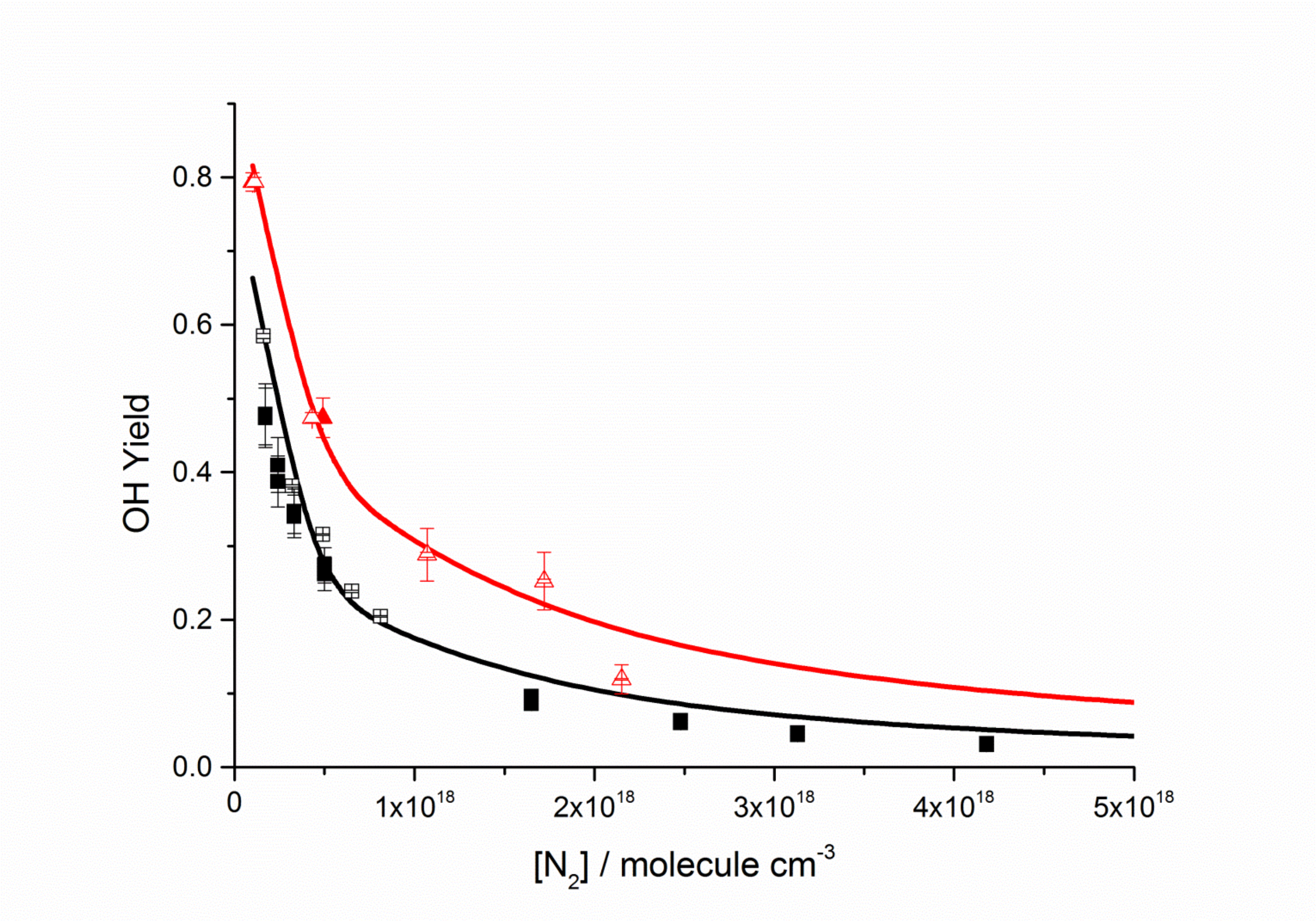

Figure 7. Results from absolute (filled) and relative (open) OH radical yield measurements of $CH_3OCH_2 + O_2$ reaction (R2) versus [N_2] at 295 (black squares) and 450 K (red triangles). The solid lines correspond to master equation calculations with the hindered rotor model.

Values of k_M/k_C were determined as a function of temperature using both helium and nitrogen buffer gases employing two independent methods (relative and absolute) and with different methods of radical generation. In general, the values of k_M/k_C from these determinations agree within the combined uncertainties, particularly at 195 and 295 K. This good agreement verifies the assumption made in defining equation 2 that the yield of $[CH_3OCH_2]_0$ from the photolysis and subsequent thermalisation is independent of pressure, within the experimental uncertainty. In addition, the intercept, $1/\alpha$ from the absolute method is compatible, within experimental error, with the value of unity assumed in the relative yield determinations, demonstrating that OH is the dominant product at zero pressure. However, while the relative method still produced consistent results for k_M/k_C at 450 K, at this temperature agreement with the absolute method was less good. With OH generated directly from t-butyl hydroperoxide, the value of k_M/k_C, $(0.39 \pm 0.04) \times 10^{-18}$ cm^3, is similar to the average of the relative methods, $(0.62 \pm 0.17) \times 10^{-18}$ cm^3. However, values of k_M/k_C determined with the more indirect oxalylchloride/DME method give values more than a factor two greater than the average of the relative methods. We prefer our values obtained with the relative method, because the absolute data are obtained over a much longer timescale (~10 ms) than the relative yield data (~0.5 ms) and hence there is potential for interference from unknown secondary chemistry in the longer timescale experiments.

4. Theoretical Methods

4.1 Electronic structure calculations

The stationary points on the $CH_3OCH_2 + O_2$ surface were characterised by calculations at the CBS-Q//MPW1K/ aug-cc-pVTZ level of theory using the Gaussian 03 suite of *ab initio* software. The resulting surface is shown in Figure 8. Various other levels of theory were explored but it was found that, when performing the statistical rate theory calculations, the CBS-Q//MPW1K/aug-cc-pVTZ energy for RO_2 ($CH_3OCH_2O_2$) gave the best agreement between experiment and theory. As discussed below, there are large variations in the energies of the different transition states with different levels of theory and the energies for these were ultimately varied in order to fit the experimental data as will be described in Section 5. Hessian matrices were also calculated at the MPW1K/ aug-cc-pVTZ level of theory in order to obtain harmonic frequencies for each species. The connectivity between wells and transitions state was confirmed by intrinsic reaction co-ordinate calculations at the MPW1K/ aug-cc-pVTZ level of theory. The structures of the important species are shown in the supplementary information.

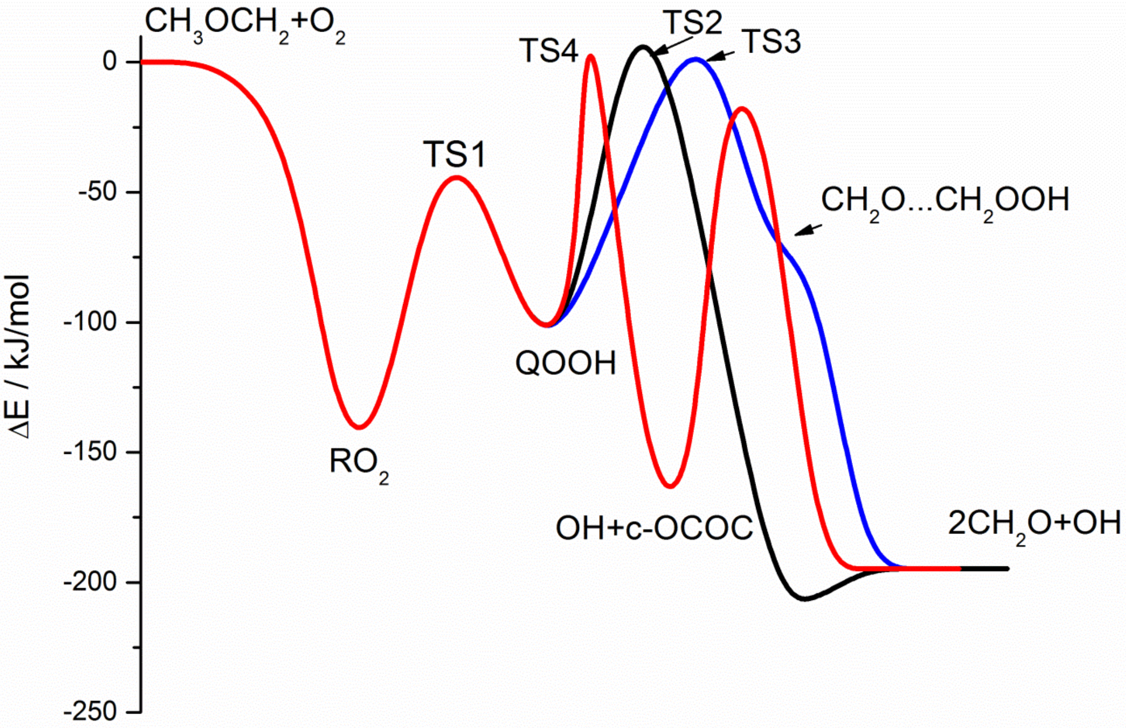

Figure 8. Schematic of the CH_3OCH_2/O_2 potential energy surface calculated at the CBS-Q//MPW1K/aug-cc-pVTZ level. RO_2 = $CH_3OCH_2O_2$, QOOH = CH_2OCH_2OOH, c-OCOC = cyclic(OCH_2OCH_2).

It is noted that there appears to be significant multireference character in the region of both TS1 and TS2/3/4 and for all transition states different composite model chemistries, all of which would be expected to reproduce the correct energy to within 4-8 kJ mol^{-1}, instead yield an energy range of ~26 kJ mol^{-1} for TS1 and ~40 kJ mol^{-1} for transition states in the TS2/3/4 region. These results are shown in Table 2 and it is noticed that the energies are particularly sensitive to the levels of theory used to perform the geometry optimisations. The geometries of the different stationary points are shown in Figure S1 of the supplementary information. Commonly, the extent to which a species is affected by multireference character can be explored by the T_1 diagnostic developed by Lee and Taylor.[45] These diagnostic values were calculated using Molpro[46] at the CCSD(T)-F12/VTZ-F12 level of theory and are also shown in Table 2. A T_1 diagnostic of > 0.02 indicates problems with a single reference wavefunction and the result for TS2 in particular is well in excess of this.

Table 2. Energies for TS1, 2 3 and 4 (including ZPE correction) in kJ mol^{-1} calculated at different levels of theory.

	G4//B3LYP/ 6-311G(d,p)	G4//MP2(full) /6-311G(d,p)	CBS-Q //MP2 /6-311G(d,p)	CBS-Q //MPW1K/ aug-cc-pVTZ	CBS-APNO// MPW1K/ aug-cc-pVTZ	RCCSD(T)-F12/VTZ-F12// MPW1K/aug-cc-pVTZ	T_1 diagnostic
TS1	-32.4	-46.8	-58.1	-41.2	-44.8	-31.8	0.019
TS2	4.1	30.5	39.8	12.3	10.0	0.1	0.036
TS3	7.7	10.6	7.7	5.0	5.0	9.1	0.026
TS4	16.8	33.1	24.4	8.1	-0.7	9.2	0.023

4.2 Master Equation Calculations

The form of the energy grained master equation (ME) used in this work has been described in detail previously.[47-49] Collisional energy transfer and isoenergetic inter-conversion between species was described with a set of coupled differential equations. Briefly, the form used in this work is:

$$\frac{\mathrm{d}}{\mathrm{dt}}\mathbf{p} = \mathbf{Mp} \qquad \text{(E9)}$$

where **p** is the population vector containing the populations, $p_i(E,t)$, of the energy grains, i refers to the ith isomer, and **M** is the matrix that determines grain population evolution due to collisional energy transfer and reaction. Two isomers, $CH_3OCH_2O_2$ (RO_2) and CH_2OCH_2OOH (QOOH), were included in the calculation. The phase space for each isomer was divided into energy grains with a width of 50 cm^{-1}. **p** contains an additional element that represents the minority reactant, CH_3OCH_2; [O_2] was in great excess and its concentration was incorporated in the pseudo-first-order rate constant for reaction of CH_3OCH_2.

Collisional energy transfer was described using an exponential down model, parameterised with the appropriate Lennard-Jones parameters and the average energy transferred in a downward direction, $\langle \Delta E \rangle_{\text{down}}$. The $\langle \Delta E \rangle_{\text{down}}$ parameter was determined using a least squares fit to the experimental data, as discussed below.

For the barrierless, methoxymethyl + O_2 reaction and the reverse dissociation, conventional transition state theory is not appropriate because the location of the transition state is not fixed, but varies along the reaction coordinate as function of energy, a situation which is typical of association reactions between open shell species.[50] In principle such reaction can be treated by variational transition state methods, however, such methods demand accurate knowledge of the potential energy surface along and orthogonal to the reaction coordinate. The association *k*(*E*)s have been calculated using a more pragmatic approach, by taking the Inverse Laplace Transform (ILT) of the modified Arrhenius form of the experimental high pressure association rate coefficient to derive the sum of states, *W*(*E*), for the association transition state.[49,51] In this work, the form of the modified Arrhenius expression used was:

$$k_a(T) = A\left(\frac{T}{T_0}\right)^n \exp(-E_a/(k_b T)) \tag{E10}$$

where T_0 was set to 293 K. E_a was set to 0 kJ mol^{-1}, i.e., supported by the electronic structure calculations, the association was assumed barrierless. Both *A* and *n* were left as variable parameters, and were determined according to a least squares fit to the experimental data. The fitting methodology is discussed in further detail below. For each ME calculation performed in this work, the discretized matrix **M** was diagonalized, and the eigenpairs were determined to give a solution of the form:

$$\mathbf{p}(t) = \mathbf{U}e^{\Lambda t}\mathbf{U}^{-1}\mathbf{p}(0) \tag{E11}$$

where **p**(0) contains the initial conditions (i.e., at $t = 0$) for each grain (i.e., $p_i(E,0)$), **U** is a matrix of eigenvectors obtained from diagonalization of **M**, and **Λ** is a diagonal matrix of the corresponding eigenvalues. Within our formulation of the ME, products are represented using the infinite sink approximation.[35]

There are three chemically significant eigenvalues, $\lambda_1 - \lambda_3$, closely related in magnitude to the reciprocal lifetimes of RO_2 ($CH_3OCH_2O_2$), CH_3OCH_2 and QOOH($CH_2OCH_2O_2H$), in order of decreasing lifetime (see Supplementary Information). λ_3 is too large in magnitude, and the impact of related reactions have too small an impact on [OH], to be observed under any of the conditions examined experimentally. Over the temperature range 195 – 450 K, the OH profile provides a direct measurement of λ_2, while λ_1 corresponds to timescales which are much longer than that of the experiments. At temperatures above 550 K the magnitude of λ_1 is such that the reactions of RO_2 occur on the experimental timescale and contribute to the secondary OH formation shown in Figure 2. At temperatures above 650 K (i.e. above the range investigated here) λ_1 and λ_2 approach one another in magnitude and eventually cross (see Figure S2, Supplementary Information).

In the ME analysis of the available experimental data, the calculated total loss rate coefficients (k_2) and the theoretical OH yields, obtained from fits to the time resolved species profiles at 1 ms, were fitted to the corresponding experimental quantities. The eigenvalues and yields can be obtained directly from solution of the chemical master equation. In order to obtain a complete set of phenomenological rate coefficient for the system, reactions 2 - 10, however the microcanonical information contained in the ME solution (equation 13) must be transformed using a procedure similar to that described by Bartis and Widom.[39,48] OH yields were calculated by integrating the flux (i.e. the product of the solution to equation 11 with the microcanonical rate coefficients) through those channels leading to OH, from time zero to a time equal to the experimental measurement time, which was taken to be 1 ms. The data used in the analysis are given in Tables S1 – S4 of the Supplementary Information. All ME calculations and the subsequent eigenvalue-eigenvector analysis were carried out using our recently developed MESMER (Master Equation Solver for Multi Energy-well Reactions) program, which is freely available on the web.[35]

4.3 Hindered Rotors

A key requirement for the ME/ILT/RRKM modelling of a reaction is knowledge of the density of states of the species involved in the reaction scheme. In the initial analysis, densities of states were calculated using the rigid rotor harmonic oscillator approximation. As discussed in Section 5, a subsequent set of calculations used a hindered rotor model for some intermediates and transition states. The states of a hindered rotor were calculated by representing the Hamiltonian in a basis set of one-dimensional rotor eigenfunctions and diagonalizing, as described previously.[35] Before this approach can be used a hindered rotor potential must be obtained and electronic structure theory methods were used to find the torsional potentials.

For each torsional mode the dihedral angle corresponding to the internal rotation was incremented and constrained geometry optimisations were performed at the MPW1K/6-31+G(3d,2p) level of theory as implemented by Gaussian 03.[52] The potentials from these calculations were delivered as a set of discrete points which were then fitted by a Fourier expansion which was then taken as the input potential. Finally vectors corresponding to the torsional motions were projected from the Hessian for each species, and the resulting Hessian was subsequently re-diagonalized to yield new harmonic frequencies. The methodology used has been described by Sharma, Raman and Green.[53]

Torsions were included for CH_3OCH_2, RO_2, QOOH, TS2, TS3 and TS4. Treatment of torsions within TS1, the cyclic TS linking RO_2 and QOOH was more problematic. There are a number of low frequency vibrational normal modes for this species which are likely to be poorly described by a harmonic oscillator model but these are less clearly identified as hindered rotations. The complications arise due to the hydrogen bonded, ring like structure which is formed as the terminal oxygen and carbon atoms co-ordinate with each other in order to undergo hydrogen transfer. Similar transition states have been considered previously and in previous publications it has been noted that the internal rotational modes in this type of molecule cannot be adequately modelled using a separable hindered rotor assumption.[53,54] In the current work we have been unable to obtain hindrance potentials for rotation about any of the bonds in TS1 and in order to probe the effect of anharmonicity within TS1, some calculations have been performed with the vibrational frequencies of this species scaled by 0.9 and 0.8 respectively relative to the other species in the system. It is noted that there is no physical justification for varying the frequencies in this way and the energy dependence of the resulting state densities is unlikely to reproduce the energy dependence from a fully coupled hindered rotational model. However, these calculations do allow an exploration of the sensitivity of the calculated results to the density of states of TS1, and give an idea of the trends expected if anharmonicity in TS1 were treated more accurately.

5. Fits to the Experimental Data

In principle the only unknown parameter in calculating the temperature and pressure dependence of the OH kinetics and yields is the energy transfer parameter, $\langle \Delta E \rangle_{\text{down}}$, used in the ME calculations. Potentially the ILT parameters could also be treated as unknowns; however, since the experimental kinetics measurements appear to reach the high pressure limit at 195 and 293 K, these values were used to constrain the ILT A factor, giving an value for A of 1.03×10^{-11} cm^3 molecule^{-1} s^{-1}. The ILT $n\infty$ parameter (equation 10) was allowed to vary. Initial calculations, using typical values of $\langle \Delta E \rangle_{\text{down}}$, were unable to reproduce the experimental data and the uncertainties in the transition state energies suggest that these too should be considered as variable parameters. The large quantity of experimental data allows for the realistic investigation of a number of parameters.

Comparison to the experimental data was carried out using a built-in Levenburg Marquardt fitting algorithm in MESMER, in order to minimise the merit function χ^2:

$$\chi^2 = \sum \frac{(\mathrm{k_{obs}} - \mathrm{k_{calc}})^2}{\sigma_{\mathrm{k_{obs}}}^2} \tag{E12}$$

where k_{obs} are the experimental rate coefficients for the reaction, k_{calc} are the corresponding calculated rate coefficients and $\sigma_{k\text{obs}}$ is the experimental error. In these calculations a temperature dependence was used as given by the following equation:

$$< \Delta E >_{\mathrm{down}} = < \Delta E >_{\mathrm{down,ref}} \left(\frac{T}{298}\right)^{d} \qquad \text{(E13)}$$

and both $\langle \Delta E \rangle_{\mathrm{down,ref}}$ and the exponent d were fitted for both the He and N_2 bath gas experiments giving a total of four parameters. In all calculations $\langle \Delta E \rangle_{\mathrm{down}}$ was constrained to be identical for both RO_2 and QOOH. The energies of both TS1 and TS3 were also allowed to vary in the fitting calculations, and the difference between the energies of TS3 and TS2, and TS3 and TS4 were constrained at the ab initio values such that the energies of all three of the transition states to OH formation varied simultaneously and equally. The calculated energies for RO_2 and QOOH were used unchanged. The vibrational and energetic properties of the different species are given in Table S6 of the Supplementary Information. For those wishing more detailed information, an example MESMER input file is also included in the supplementary information and the hindrance potentials for each species may be found there with each potential enclosed by the xml element <me:HinderedRotorPotential …… <me:HinderedRotorPotential/>.

The fitting calculations were carried out for both a hindered rotor model and a harmonic oscillator only model. Additionally given the hindered rotor considerations described above for TS1, further models were used in which the vibrational densities of states were scaled by 0.9 and 0.8. These results are shown in Table 3 with 1σ errors taken from the diagonal elements of the correlation matrix. In these fitting calculations the statistical 2σ errors for each measurement were used and an additional 5% error was propagated with these in order to account for non-statistical sources of error.

It is apparent from these calculations that in all cases it is necessary to substantially reduce the barrier heights corresponding to TS1 and TS3 (ab initio energies of -41.2 and 5.0 kJ mol^{-1} for TS1 and TS3 respectively at the CBS-Q //MPW1K/ aug-cc-pVTZ level). Normally an error of ~±4 kJ mol^{-1} [55] would be considered appropriate for the CBS-QB level of theory; however, in this case, the significant multireference character in the vicinity of these transition states raises questions over the reliability of the CBS-QB energies.

Table 3. Optimised parameters for the $CH_3OCH_2 + O_2$ system from fitting calculations in MESMER. Errors are given at the 1σ level from the fitting calculations with an additional 5 % error propagated with the statistical error for each experimental point.

	Hindered Rotor	Harmonic oscillator	Hindered rotors TS1 ν scaled by 0.9	Hindered rotors TS1 ν scaled by 0.8	Ab initio calculation
RO_2 / kJ mol^{-1}	-	-	-	-	-145.46
QOOH / kJ mol^{-1}	-	-	-	-	-100.32
$\langle \Delta E \rangle_{\mathrm{down,ref}}$ (He) / cm^{-1}	173 ± 11	289 ± 9	165 ± 4	181 ± 5	-
d(He)	-0.02 ± 0.37	-0.05 ± 0.11	-0.10 ± 0.07	-0.10 ± 0.9	-
$\langle \Delta E \rangle_{\mathrm{down,ref}}$ (N_2) / cm^{-1}	523 ± 53	1640 ± 200	486 ± 24	576 ± 32	-
d(N_2)	0.01 ± 0.17	-0.72 ± 0.48	-0.06 ± 0.25	-0.13 ± 27	-
TS1 / kJ mol^{-1}	-56.7 ± 1.0	-50.2 ± 1.5	-47.8 ± 0.8	-42.0 ± 0.4	-41.2
TS3 / kJmol^{-1}	-34.5 ± 0.6	-25.9 ± 0.5	-38.0 ± 1.2	-47.6 ± 4.2	5.0
ILT n	-0.67 ± 0.13	-0.64 ± 0.13	-0.75 ± 0.12	-0.90 ± 0.09	-
(Minimum χ^2) / No. of degrees of freedom	1.2	1.2	1.2	1.1	-

Furthermore, it was found that the fitted barrier heights depend strongly upon the way in which the vibrational degrees of freedom are treated. A purely harmonic treatment gives transition state energies for TS1 which are closer to the ab initio data than are those from a more physically realistic hindered rotor treatment. However, as has been noted above, the treatment of anharmonicity in TS1 raises significant problems in this system and, while no hindered rotational potentials have been obtained for this species, the low frequency vibrations are likely to be poorly described by a harmonic oscillator approximation. By treating hindered rotations in all species other than TS1, the density of states within TS1 will then be artificially low relative to that for the other species, whereas in the harmonic oscillator only model there could be some degree of cancellation of error due to the density of states of RO_2 being treated on the same basis as those in TS1. In support of this rationale it can be seen that when increasing the densities of states of TS1 by scaling the vibrational frequencies, the fitted energy of TS1 is increased, in better agreement with the ab initio result.

From the χ^2 values in Table 3 of 1.2 for both the hindered rotor and harmonic oscillator models respectively, it can be demonstrated that both models yield equally good agreement with the experimental data. However the main deficiency in the harmonic oscillator only model concerns the fitted values for $\langle\Delta E\rangle_{\mathrm{down}}$. The harmonic oscillator model requires a large $\langle\Delta E\rangle_{\mathrm{down,ref}}$(He) in order to fit the data of (289 ± 9) cm^{-1} compared to (173 ± 11) cm^{-1} for the hindered rotor model. Considering other reaction systems with a He bath gas, a value of 289 cm^{-1} seems unreasonably large compared to typical values of around 100 - 200 cm^{-1}. [47,49,56,57] With a nitrogen bath gas the situation is exacerbated with a $\langle\Delta E\rangle_{\mathrm{down,ref}}$($N_2$) of 1643 cm^{-1} required in order to fit the data with a harmonic oscillator model compared to a value of 523 cm^{-1} for the hindered rotor model. It can also be seen that the harmonic model gives a significantly negative temperature dependence for $\langle\Delta E\rangle_{\mathrm{down,ref}}$($N_2$) which is unrealistic. It is noted that the hindered model also gives a slightly negative temperature dependence to $\langle\Delta E\rangle_{\mathrm{down,ref}}$($N_2$) , but in this case it is temperature independent within error. The reason for the difference between models is likely due to the fact that CH_3OCH_2 has two internal rotors, while RO_2 has three (See Figure S1, Supplementary Information). As a result, the harmonic oscillator model would be expected to under predict the densities of states of RO_2 relative to those of CH_3OCH_2. From these results we can conclude that the more physically realistic hindered rotor model is necessary to model the $CH_3OCH_2 + O_2$ system.

The experimental yields and measurements of k_2 with a He bath gas are compared with theoretical values using the hindered rotor model in Figures 9a and 9b and it is demonstrated that good agreement is obtained.

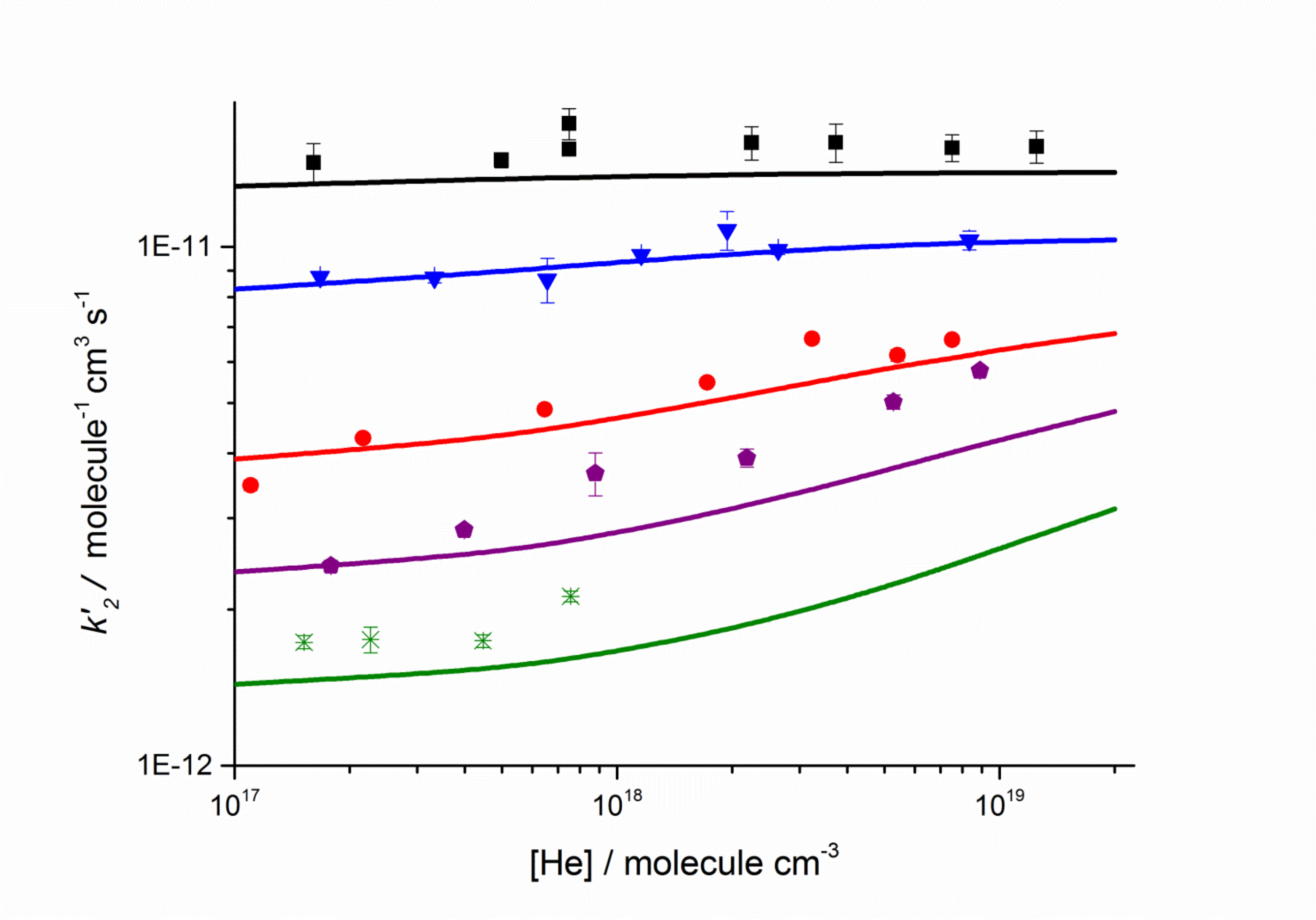

Figure 9a. Comparison between experimental and theoretical rate coefficients (k_2) with theoretical data obtained from MESMER using the best fit parameters from the hindered rotor model (solid line). The black squares, blue triangles, red circles, purple hexagons and stars, correspond to data at 195 K, 298 K, 450 K, 550 K and 650 K respectively.

Experiments in the temperature range 550 – 650 K range provide information on λ_1, as shown in Figure 3. These data were also used in the fits. As discussed above, the main contributor to this eigenvalue is formation of OH by well-skipping from RO_2 (k_{9b}), with smaller contributions from reaction sequences initiated by reactions 9a and 9c. The simulated eigenvalues were fitted to the experimental eigenvalues, so that all of these processes were automatically and appropriately included in the fits. The most sensitive parameter was the energy of TS2.

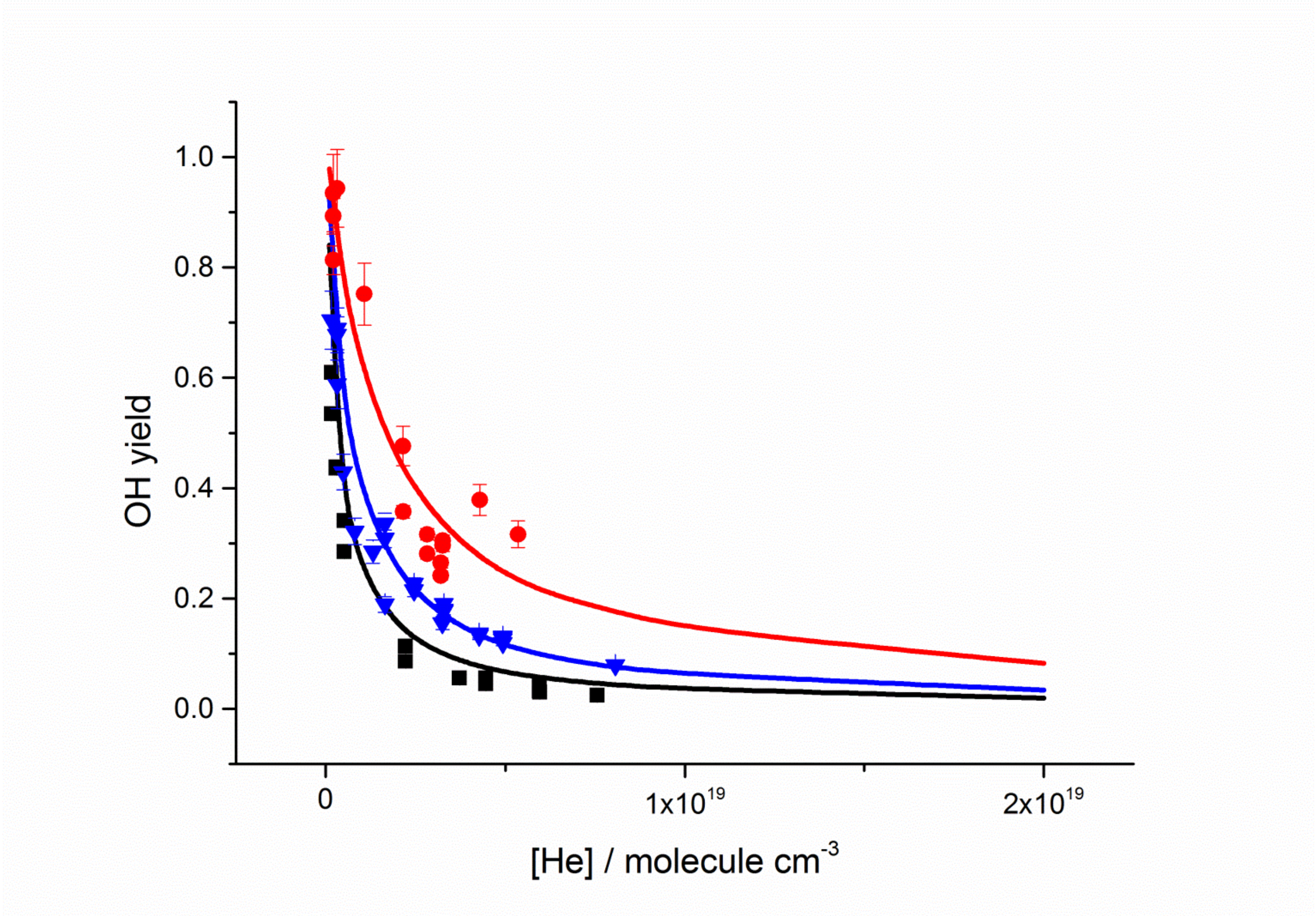

Figure 9b. Comparison between experimental and theoretical OH yields with theoretical data obtained from MESMER using the best fit parameters from the hindered rotor mode (solid line). The black squares, blue triangles and red circles correspond to data at 195 K, 298 K, and 450 K, respectively.

The λ_1 values from the best fit hindered rotor model are compared with the experimental values in Figure 10. The modelled eigenvalue underestimates the experimental value at the lowest temperature by a factor of 2-3. A contribution to secondary OH formation via reaction of QOOH with O_2 to form a peroxyhydroperoxy radical, followed by dissociation, provides a possible explanation of this discrepancy:

$$QOOH + O_2 \rightarrow O_2CH_2OCH_2OOH\ (O_2QOOH) \qquad (R11)$$

$$O_2CH_2OCH_2OOH\ (O_2QOOH) \rightarrow HO_2CH_2OCHO + OH \qquad (R12)$$

$$HO_2CH_2OCHO \rightarrow OCH_2OCHO + OH \qquad (R13)$$

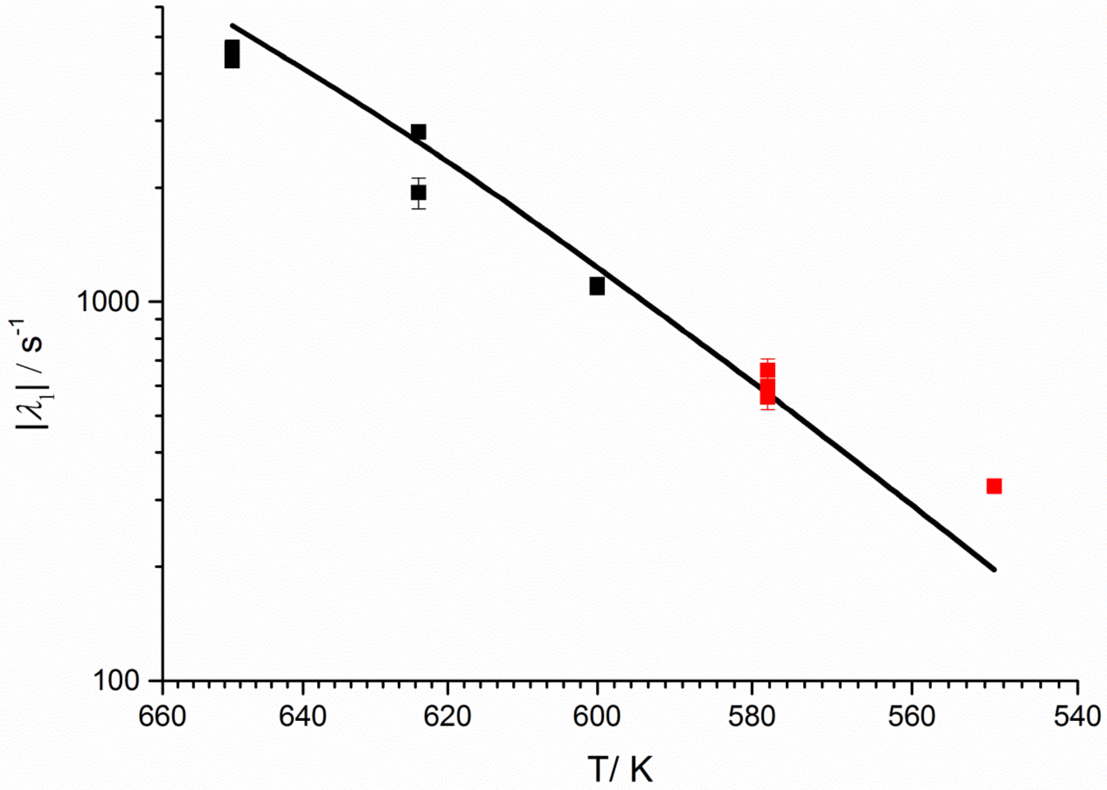

Figure 10. Arrhenius plot of eigenvalue λ_{e1}, comparing best fit from the master equation analysis (line) and experimental values. The lowest temperature points (shown in red) were not included in the fits for reasons discussed in the text.

These reactions provide the branching steps in DME autoignition mechanisms. The last step, reaction 13, is too slow to contribute on the timescales of the present experiments at 550 K, but it is found that reaction 12 rapidly follows reaction 11, leading to production of a single OH under our conditions. Simulations of the secondary OH time profile, using these reactions in addition to OH formation from RO_2, adequately explain the discrepancy, and provide the required increase in the rate of OH formation on the required timescale, using the value for k_{11} proposed by Fischer et al.[12] These simulations are discussed in more detail below. Since k_{11} is independent of temperature, the contribution of this route to secondary OH formation in our experiments is unimportant at 600 K and above, as shown in Figure 10, because of the rapid increase in λ_1, while $k_{11}[O_2]$ is independent of T (in all cases the contribution was less than 10%). Accordingly, the datapoints at 550 and 578 K were omitted from the master equation fits. For the purpose of representing the individual pressure and temperature dependent rate coefficients from the best fit ME model, we have fitted them with Chebyshev polynomials using the methodology described by Naik and co-workers[58] which has been automated in MESMER. The method and the results are given in the Supplementary Information tables S7 to S15 for He and for S16 to S24 for N_2.

6. Application of rate coefficients to DME ignition chemistry

A crucial issue in determining the ignition chemistry of DME is the competition between addition of O_2 to QOOH and QOOH decomposition, either to form OH (reaction 10b), or to regenerate RO_2 (reaction 10c). The latter reaction substantially decreases the steady state concentration of QOOH, thus limiting the rate of the dissociation reaction. Disagreement exists as to the exact chain branching mechanism,[34,59,60,14] but ignition is postulated to occur via the production of O_2QOOH followed by subsequent isomerization's and chain branching decompositions, as discussed briefly above. Well-skipping reactions, which do not significantly sample the QOOH well, are important at lower pressures and will reduce the yield of O_2QOOH, whereas, at high pressures, excited QOOH species will be stabilized. Numerical integration by Fischer, Dryer and Curran[12,13] (FDC) has been used to explore this reaction system, but the current work offers more information on the elementary rate coefficients than was previously available. Specifically the FDC model does not include the pressure dependence of the elementary rate coefficients or rate data for the well-skipping reactions. The full mechanism obtained from the Bartis Widom analysis consists of reactions 2, 9, 10. The well-skipping reactions are 2b, 2c, 9b, 10a.

Using the nine rate coefficients for reactions 2, 9 and 10 from the master equation calculations with the best fit parameters from the hindered rotor model, the numerical integration software Kintecus[61] was used in order to predict the importance of chain branching from reaction of O_2 with QOOH. Reactions 11-13 were also included from the FDC model with the slightly modified more recent values for the rate coefficients from Zhao et al.[14]

The Arrhenius parameters for these reactions are given in Table 4. Numerical integrations were performed under the conditions at which experimental eigenvalues for secondary OH formation were obtained and from these calculations the time resolved concentrations of the component species could be obtained with and without the additional QOOH + O_2 chemistry. Examples of the simulated time profiles at 550 K are shown in Figure 11 including simulations with both the FDC value for the QOOH + O_2 rate coefficient (1.16×10^{-12} molecule^{-1} cm^3 s^{-1}) and a doubled value of 2.32×10^{-12} molecule^{-1} cm^3 s^{-1}. It is noted that there is likely a large uncertainty in the value for the QOOH + O_2 rate coefficient. This figure suggests that the sequence of reactions initiated by QOOH + O_2 (reaction 11) provides an explanation of the underestimation of the rate of secondary OH formation by the MESMER model of the R + O_2 system at 550 K. Further, more direct studies, are currently in progress.

Table 4. Arrhenius parameters for key branching reaction from Zhao et al.[14]

	A / (molecule^{-1} cm^3)^a s^{-1}	n	Ea / kJ mol^{-1}
QOOH + O_2 → O_2QOOH[b]	1.16×10^{-12}	0.00	0.00
O_2QOOH → HO_2CH_2OCHO+OH	4.00×10^{10}	0.00	77.3
HO_2CH_2OCHO → OCH_2OCHO+OH	3.00×10^{16}	0.00	167.2

[a]units for *A* are s^{-1} in the case of unimolecular reactions and cm^3 molecule^{-1} s^{-1} in the case of the bimolecular QOOH + O_2 reaction. [b]O_2QOOH = $O_2CH_2OCH_2OOH$.

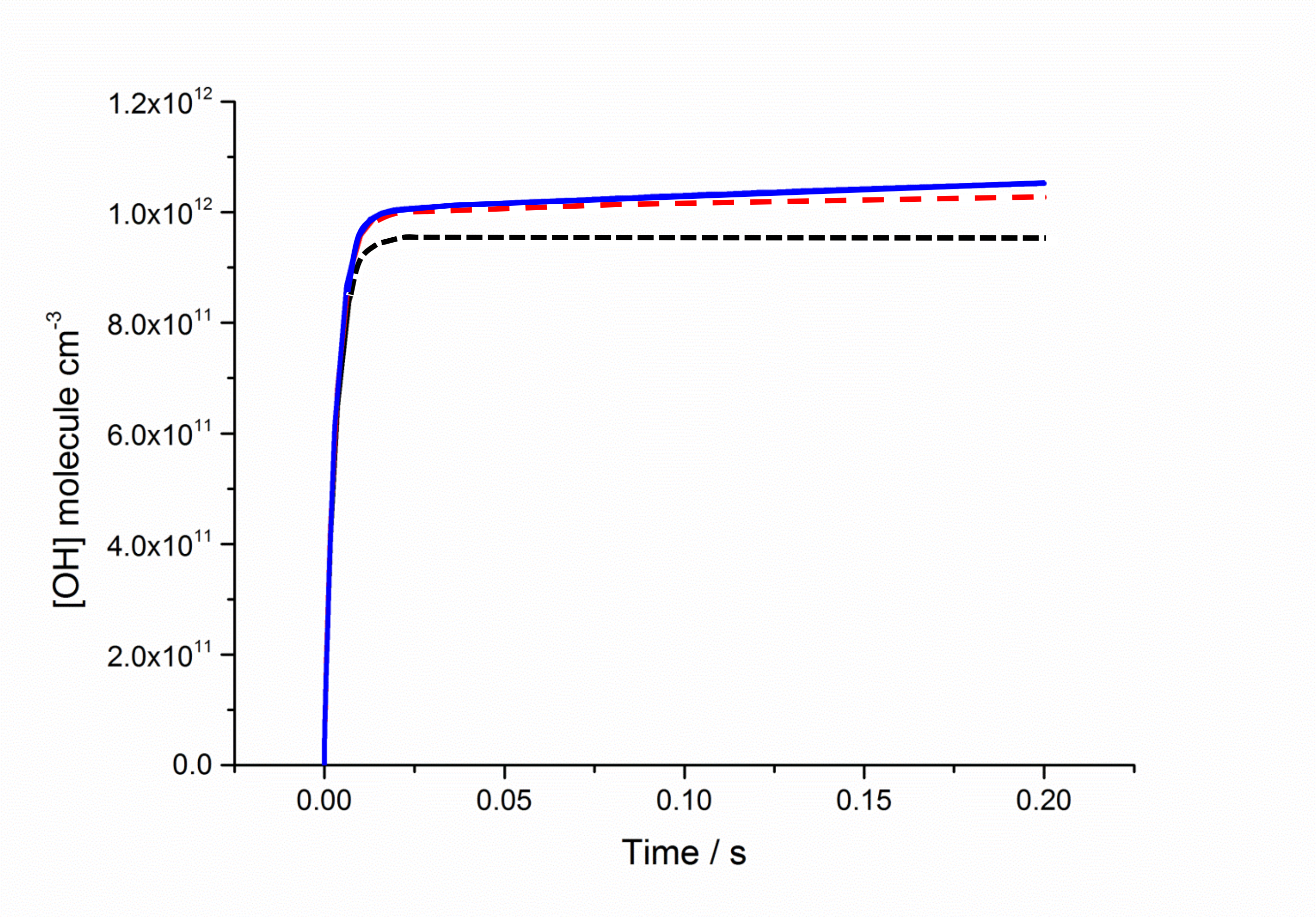

Figure 11. Modelling of OH profiles using a model based upon MESMER rate coefficients (reactions 2, 9 and 10) from the current work at 550 K and 500 Torr with $[O_2] = 1\times10^{17}$ molecule cm^{-3}. These use different values for the QOOH + O_2 rate coefficient of 0 (black short dashed line), 1.16×10^{-12} (red long dashed line) and 2.32×10^{-12} (blue solid line) molecule^{-1} cm^3 s^{-1}.

In order to demonstrate the differences between the current model and that used by FDC additional numerical integrations have been performed comparing simulated concentrations of the QOOH-O_2 adduct (O_2QOOH), using the full MESMER model plus reactions 11-13 and a reduced model based on the FDC chemistry. The latter model consisted of the reactions 2a, 9a, 9c, 10b and 10c, (i.e. the mechanism listed above but without the well-skipping reactions) plus reactions 11-13, and using the pressure independent rate coefficients from FDC. These results are shown in Figure 12 for simulations at 550 K with total pressures of 1 bar and 10 bar of air. Table 5 shows the rate coefficients for reactions 9c, 10c and 11 at 550 K from the FDC model and from the Mesmer calculations.

Table 5. Rate coefficients at 1 bar and 10 bar of air for reactions 9c, 10c and 11 from the FDC model and from the master equation analysis.

	k_{9c}/s^{-1}	k_{10c}/s^{-1}	k_{11}[O$_2$] /s^{-1}
FDC (1bar)	1.6×10^2	3.7×10^5	3.8×10^6
Present model (1 bar)	1.2×10^3	6.8×10^6	3.8×10^6
FDC (10 bar)	1.6×10^2	3.7×10^5	3.8×10^7
Present model (10 bar)	1.3×10^3	7.2×10^6	3.8×10^7

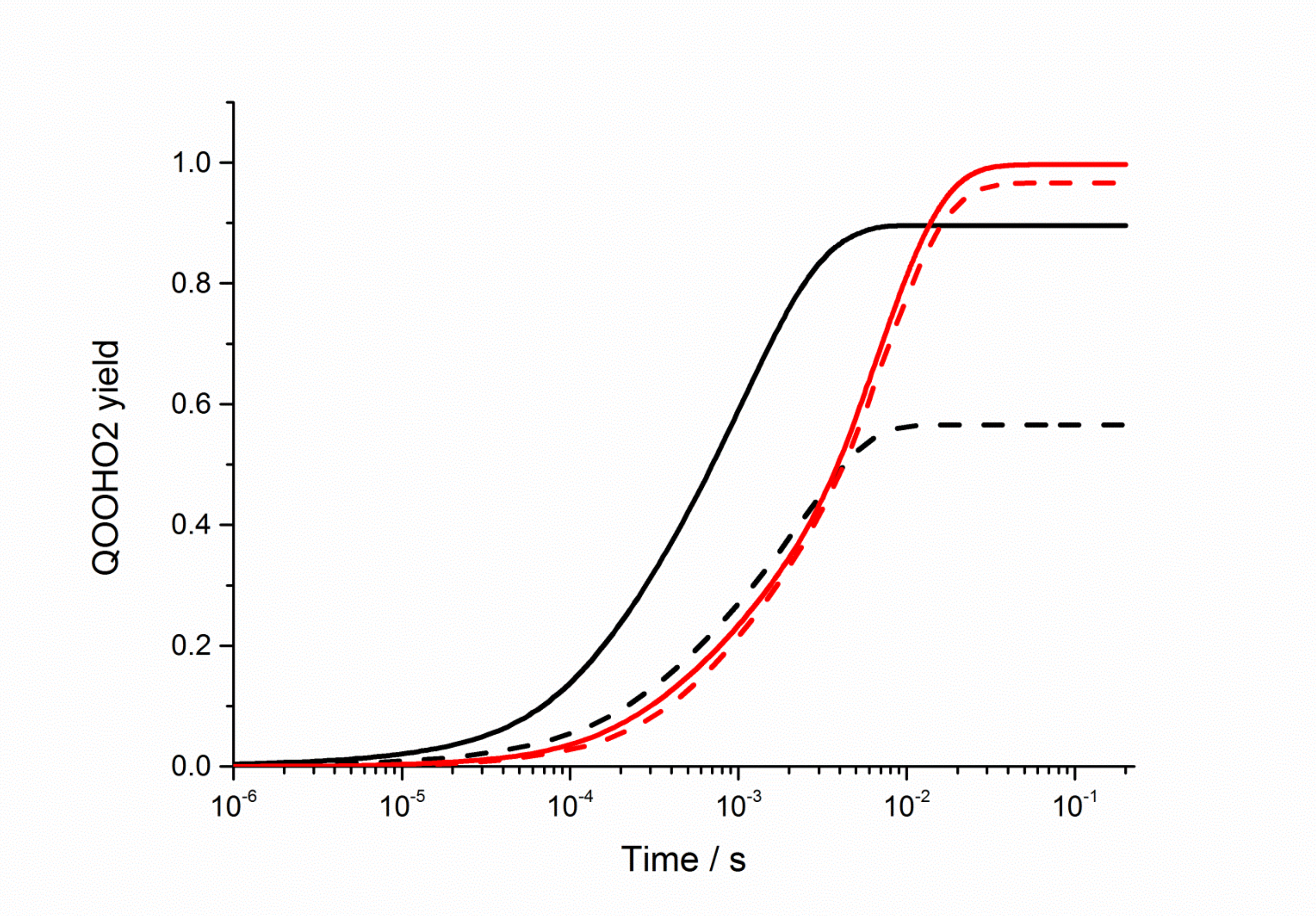

Figure 12. Modelling of O$_2$QOOH formation using a model based upon MESMER rate coefficients (2, 9 and 10) from the current work (black) at 1 bar (solid line) and 10 bar (dashed line) of air (T = 550 K). These are compared with results using rate coefficients from the FDC model (red). Time is plotted on a logarithmic scale.

Under these conditions, the timescale for formation of O_2QOOH is primarily determined by reactions whose rate coefficients are given in Table 5.

- At 1 bar, reaction 11 is the fastest reaction in this reaction sequence in the FDC model and establishes a steady-state in QOOH. The timescale of formation of O_2QOOH is determined by reaction 9c. In the model based on the master equation calculations, the energy of TS1 is much lower than that used by FDC, so that both k_{9c} and k_{10c} are substantially increased. An equilibrium between RO_2 and QOOH is established on a short timescale and the effective rate constant for formation of O_2QOOH from RO_2 becomes $(k_{9c}/ k_{10c})\ k_{11}$. The final yield of O_2QOOH is lower in the present model because of the formation of OH by well-skipping, which is not included in the FDC model. Very recent results from Kurimoto et al.[62] following HO_2, H_2O_2, DME, CO and HCHO at atmospheric pressure also suggest that less O_2QOOH is formed than the Zhao et al. model predicts. Model and measurements could be brought into better agreement by increasing the ratio of QOOH decomposition to O_2 addition, although well-skipping was not considered in this study.
- Well-skipping is suppressed at 10 bar, so the final yields of O_2QOOH are similar in both models. The timescale is unchanged in the FDC model and is still governed by k_{9c}. Formation is much faster with the master equation model and is largely determined by k_{9c}, although contributions from both k_{10c} and k_{11} reduce the timescale somewhat.

The low energy of TS1 derived from master equation fits to the experimental pulsed photolysis data clearly leads to a substantial reduction in the modelled timescale for formation of O_2QOOH, which leads on to branching reactions in the combustion of DME. The FDC mechanism successfully reproduced experimental ignition delays, suggesting that further changes are required in the mechanism to incorporate the present results and still successfully model ignition behaviour. Further experiments are in progress to examine these and related reactions under higher pressure conditions, and Tomlin et al.[63] have recently examined this issue. Note that the effects of well-skipping reactions play a significant role at lower pressures. While this result is less significant under practical combustion conditions, it can be important under laboratory conditions, where rate coefficients used in combustion modelling are frequently determined.

For the purpose of combustion modelling, the rate coefficients from the ME calculations have been represented as an expansion of Chebyshev polynomials as described in the supplementary information. These Chebyshev representations cover the temperature range from 200 to 1000 K and a density range from 1×10^{17} to 1×10^{23} molecule cm^{-3} to represent the low temperature combustion regime. It should be noted that the Chebyshev representations will not yield rate coefficients outside of these ranges. The Chebyshev coefficients are presented in the supplementary information. More detailed modelling studies will form the basis of a future publication.

7. Summary and Conclusions

1. The reaction between CH_3OCH_2 and O_2 has been studied by probing the time dependent formation of OH. Three complementary datasets were obtained:

   (i) The rate coefficient for $CH_3OCH_2 + O_2$ (k_2) over the ranges 195 – 650 K and 1 - 550 Torr.

   (ii) Eigenvalues λ_{e1} for secondary formation of OH at 550 – 650 K and 550 Torr.

   (iii) The yield of OH in reaction 2 (195 – 450 K, 1 - 550 Torr)

2. The use of OH laser induced fluorescence allowed the reaction to be studied at sufficiently low radical concentrations (~10^{11} cm^{-3}) that secondary (radical + radical) reactions were unimportant and the rate coefficients / eigenvalues could be extracted from simple bi- or tri-exponential analysis.

3. Stationary points on the potential energy surface were calculated using CBS-Q//MPW1K/ aug-cc-pVTZ level of theory.

4. The rate coefficient and OH yield data were fitted using a master equation analysis, based on the *ab initio* calculations and using a hindered rotor model. The following parameters were floated in the fits:

(i) The high pressure limit for reaction 2 was fitted using the pressure dependent data for k_2 at 195 K and 295 K, where this limit is closely approached.

(ii) $\langle \Delta E \rangle_{\mathrm{down}}$ and the energies of the transition states TS1 and TS3.

Substantial changes were required in the energies of the transition states in order to fit the experimental data, lowering them by ~20 kJ mol^{-1} (TS1) and ~ 40 kJ mol^{-1} (TS2), emphasising the importance of tuning *ab initio* calculations using experimental data for reaction systems which show substantial multireference character.

5. The best fit parameters were used to extract the nine phenomenological rate coefficients, $k_{2a\text{-}c}$, $k_{9a\text{-}c}$ and $k_{10a\text{-}c}$ from the master equation model using an analysis similar to the Bartis Widom procedure. Four of these rate coefficients relate to well-skipping reactions. The rate coefficients were fitted to Chebyshev polynomials covering the temperature range from 200 to 1000 K and the density range from 1×10^{17} to 1×10^{23} molecule cm^{-3} to represent the low temperature combustion regime.

6. Numerical integration was used in order to simulate OH formation from the QOOH + O_2 reaction. Comparison of these results with both the eigenvalues λ_1 from the master equation analysis, and the experimental time coefficients for secondary OH formation suggests that the long-time OH formation observed above 550 K has a contribution from the reaction QOOH +O_2.

7. A comparison was made with a section of the DME low temperature autoignition mechanism of Fisher, Dryer and Curran (FDC)[12]. The rate of formation of the peroxy hydroperoxy radical, O_2QOOH, a key species in the route to autoignition, was simulated. At atmospheric pressure, the well-skipping reactions depressed the yield of O_2QOOH, but these reactions were unimportant at 10 bar. The main difference was a more rapid formation of O_2QOOH with the present mechanism and this appears to be due to an increased rate of isomerisation from RO_2 to QOOH in the current model.

8. The results in this work demonstrate the use of extensive experimental data to optimise a master equation model incorporating ab initio parameters to generate an accurate parameterisation a key set of reactions in the low temperature combustion chemistry of dimethyl ether. Additionally through fitting these data, the importance of accurately treating hindered rotations is demonstrated.

Supporting Information Available

Supporting information on the analytic relations between eigenvalues and phenomenological rate coefficients, additional experimental data, molecular structure information, Chebyshev polynomials and sample MESMER input. This material is available free of charge via the Internet at http://pubs.acs.org.

Acknowledgments

AJE acknowledges support from the Academy of Finland. SAC is grateful to the EPSRC for funding a studentship. Funding for this work was provided by EPSRC grants GR/T28560/01 and EP/J010871/1.

References

(1) Arcoumanis, C.; Bae, C.; Crookes, R.; Kinoshita, E. The Potential of Di-Methyl Ether (DME) as an Alternative Fuel for Compression-Ignition Engines: A Review. *Fuel* **2008**, *87*, 1014-1030.

(2) Semelsberger, T. A.; Borup, R. L.; Greene, H. L. Dimethyl Ether (DME) as an Alternative Fuel. *J. Power Sources* **2006**, *156*, 497-511.

(3) Yan, X. Y.; Crookes, R. J. Energy Demand and Emissions from Road Transportation Vehicles in China. *Progress in Energy and Combustion Science* **2010**, *36*, 651-676.

(4) Zhang, L.; Huang, Z. Life Cycle Study of Coal-Based Dimethyl Ether as Vehicle Fuel for Urban Bus in China. *Energy* **2007**, *32*, 1896-1904.

(5) Ribeiro, N. M.; Pinto, A. C.; Quintella, C. M.; da Rocha, G. O.; Teixeira, L. S. G.; Guarieiro, L. L. N.; Rangel, M. D.; Veloso, M. C. C.; Rezende, M. J. C.; da Cruz, R. S.et al. The Role of Additives for Diesel and Diesel Blended (Ethanol or Biodiesel) Fuels: A Review. *Energy Fuels* **2007**, *21*, 2433-2445.

(6) Kim, M. Y.; Bang, S. H.; Lee, C. S. Experimental Investigation of Spray and Combustion Characteristics of Dimethyl Ether in a Common-Rail Diesel Engine. *Energy Fuels* **2007**, *21*, 793-800.

(7) Zhang, J. J.; Qiao, X. Q.; Guan, B.; Wang, Z.; Xiao, G. G.; Huang, Z. Search for the Optimizing Control Method of Compound Charge Compression Ignition (CCCI) Combustion in an Engine Fueled with Dimethyl Ether. *Energy Fuels* **2008**, *22*, 1581-1588.

(8) Dagaut, P.; Boettner, J. C.; Cathonnet, M. Chemical Kinetic Study of Dimethylether Oxidation in a Jet Stirred Reactor from 1 to 10 Atm: Experiments and Kinetic Modeling. *Proceedings of the Combustion Institute* **1996**, *26*, 627-632.

(9) Dagaut, P.; Daly, C.; Simmie, J. M.; Cathonnet, M. The Oxidation and Ignition of Dimethylether from Low to High Temperature (500-1600 K): Experiments and Kinetic Modeling. *Proceedings of the Combustion Institute* **1998**, *27*, 361-369.

(10) Dagaut, P.; Luche, J.; Cathonnet, M. The Low Temperature Oxidation of DME and Mutual Sensitization of the Oxidation of DME and Nitric Oxide: Experimental and Detailed Kinetic Modeling. *Combust. Sci. Technol.* **2001**, *165*, 61-84.

(11) Mittal, G.; Chaos, M.; Sung, C. J.; Dryer, F. L. Dimethyl Ether Autoignition in a Rapid Compression Machine: Experiments and Chemical Kinetic Modeling. *Fuel Processing Technology* **2008**, *89*, 1244-1254.

(12) Fischer, S. L.; Dryer, F. L.; Curran, H. J. The Reaction Kinetics of Dimethyl Ether. I: High-Temperature Pyrolysis and Oxidation in Flow Reactors. *Int. J. Chem. Kinet.* **2000**, *32*, 713-740.

(13) Curran, H. J.; Fischer, S. L.; Dryer, F. L. The Reaction Kinetics of Dimethyl Ether. II: Low-Temperature Oxidation in Flow Reactors. *Int. J. Chem. Kinet.* **2000**, *32*, 741-759.

(14) Zhao, Z.; Chaos, M.; Kazakov, A.; Dryer, F. L. Thermal Decomposition Reaction and a Comprehensive Kinetic Model of Dimethyl Ether. *Int. J. Chem. Kinet.* **2008**, *40*, 1-18.

(15) Gao, J.; Nakamura, Y. Two-Stage Ignition of DME/Air Mixture at Low-Temperature (< 500 K) under Atmospheric Pressure. *Fuel* **2013**, *106*, 241-248.

(16) Herrmann, F.; Osswald, P.; Kohse-Hoinghaus, K. Mass Spectrometric Investigation of the Low-Temperature Dimethyl Ether Oxidation in an Atmospheric Pressure Laminar Flow Reactor. *Proceedings of the Combustion Institute* **2013**, *34*, 771-778.

(17) Pfahl, U.; Fieweger, K.; Adomeit, G. Self-Ignition of Diesel-Relevant Hydrocarbon-Air Mixtures under Engine Conditions. *Proceedings of the Combustion Institute* **1996**, *26*, 781-789.

(18) Cook, R. D.; Davidson, D. F.; Hanson, R. K. Shock Tube Measurements of Ignition Delay Times and OH Time-Histories in Dimethyl Ether Oxidation. *Proceedings of the Combustion Institute* **2009**, *32*, 189-196.

(19) Li, Z. H.; Wang, W. J.; Huang, Z.; Oehlschlaeger, M. A. Dimethyl Ether Autoignition at Engine-Relevant Conditions. *Energy Fuels* **2013**, *27*, 2811-2817.

(20) Xu, H. J.; Yao, C. D.; Yuan, T.; Zhang, K. W.; Guo, H. J. Measurements and Modeling Study of Intermediates in Ethanol and Dimethy Ether Low-Pressure Premixed Flames Using Synchrotron Photoionization. *Combust. Flame* **2011**, *158*, 1673-1681.

(21) Wang, J.; Chaos, M.; Yang, B.; Cool, T. A.; Dryer, F. L.; Kasper, T.; Hansen, N.; Osswald, P.; Kohse-Hoinghaus, K.; Westmorelande, P. R. Composition of Reaction Intermediates for Stoichiometric and Fuel-Rich Dimethyl Ether Flames: Flame-Sampling Mass Spectrometry and Modeling Studies. *Phys. Chem. Chem. Phys.* **2009**, *11*, 1328-1339.

(22) Zador, J.; Taatjes, C. A.; Fernandes, R. X. Kinetics of Elementary Reactions in Low-Temperature Autoignition Chemistry. *Progress in Energy and Combustion Science* **2011**, *37*, 371-421.

(23) Cook, R. D.; Davidson, D. F.; Hanson, R. K. High-Temperature Shock Tube Measurements of Dimethyl Ether Decomposition and the Reaction of Dimethyl Ether with OH. *J. Phys. Chem. A* **2009**, *113*, 9974-9980.

(24) Carr, S. A.; Still, T. J.; Blitz, M. A.; Eskola, A. J.; Pilling, M. J.; Seakins, P. W.; Shannon, R. J.; Wang, B.; Robertson, S. H. Experimental and Theoretical Study of the Kinetics and Mechanism of the Reaction of OH Radicals with Dimethyl Ether. *J. Phys. Chem. A* **2013**, *117*, 11142-11154.

(25) Bansch, C.; Kiecherer, J.; Szori, M.; Olzmann, M. Reaction of Dimethyl Ether with Hydroxyl Radicals: Kinetic Isotope Effect and Prereactive Complex Formation. *J. Phys. Chem. A* **2013**, *117*, 8343-8351.

(26) Masaki, A.; Tsunashima, S.; Washida, N. Rate Constants for Reactions of Substituted Methyl Radicals (CH_2OCH_3, CH_2NH_2, CH_2I, and CH_2CN) with O_2. *J. Phys. Chem.* **1995**, *99*, 13126-13131.

(27) Hoyermann, K.; Nacke, F. Elementary Reactions of the Methoxymethyl Radical in the Gas Phase: CH_3OCH_3+F, CH_2OCH_3+CH_2OCH_3, CH_2OCH_3+O_2 and CH_2OCH_3+O. *Proceedings of the Combustion Institute* **1996**, *26*, 505-512.

(28) Sehested, J.; Sehested, K.; Platz, J.; Egsgaard, H.; Nielsen, O. J. Oxidation of Dimethyl Ether: Absolute Rate Constants for the Self Reaction of CH_3OCH_2 Radicals, the Reaction of CH_3OCH_2 Radicals with O_2, and the Thermal Decomposition of CH_3OCH_2 Radicals. *Int. J. Chem. Kinet.* **1997**, *29*, 627-636.

(29) Maricq, M. M.; Szente, J. J.; Hybl, J. D. Kinetic Studies of the Oxidation of Dimethyl Ether and Its Chain Reaction with Cl_2. *J. Phys. Chem. A* **1997**, *101*, 5155-5167.

(30) Rosado-Reyes, C. M.; Francisco, J. S.; Szente, J. J.; Maricq, M. M.; Ostergaard, L. F. Dimethyl Ether Oxidation at Elevated Temperatures (295-600 K). *J. Phys. Chem. A* **2005**, *109*, 10940-10953.

(31) Eskola, A. J.; Carr, S. A.; Blitz, M. A.; Pilling, M. J.; Seakins, P. W. Kinetics and Yields of OH Radical from the CH_3OCH_2 + O_2 Reaction Using a New Photolytic Source. *Chem. Phys. Lett.* **2010**, *487*, 45-50.

(32) Yamada, T.; Bozzelli, J. W.; Lay, T. H. Comparisons of CBS-Q and G2 Calculations on Thermodynamic Properties, Transition States, and Kinetics of Dimethyl-Ether Plus O_2 Reaction System. *Int. J. Chem. Kinet.* **2000**, *32*, 435-452.

(33) Sehested, J.; Mogelberg, T.; Wallington, T. J.; Kaiser, E. W.; Nielsen, O. J. Dimethyl Ether Oxidation: Kinetics and Mechanism of the CH_3OCH_2+O_2 Reaction at 296 K and 0.38-940 Torr Total Pressure. *J. Phys. Chem.* **1996**, *100*, 17218-17225.

(34) Andersen, A.; Carter, E. A. First-Principles-Derived Kinetics of the Reactions Involved in Low-Temperature Dimethyl Ether Oxidation. *Mol. Phys.* **2008**, *106*, 367-396.

(35) Glowacki, D. R.; Liang, C. H.; Morley, C.; Pilling, M. J.; Robertson, S. H. MESMER: An Open-Source Master Equation Solver for Multi-Energy Well Reactions. *J. Phys. Chem. A* **2012**, *116*, 9545-9560.

(36) Carr, S. A.; Baeza-Romero, M. T.; Blitz, M. A.; Pilling, M. J.; Heard, D. E.; Seakins, P. W. OH Yields from the CH_3CO+O_2 Reaction Using an Internal Standard. *Chem. Phys. Lett.* **2007**, *445*, 108-112.

(37) Carr, S. A.; Baeza-Romero, M. T.; Blitz, M. A.; Price, B. J. S.; Seakins, P. W. Ketone Photolysis in the Presence of Oxygen: A Useful Source of OH for Flash Photolysis Kinetics Experiments. *Int. J. Chem. Kinet.* **2008**, *40*, 504-514.

(38) Carr, S. A.; Blitz, M. A.; Seakins, P. W. Site-Specific Rate Coefficients for Reaction of OH with Ethanol from 298 to 900 K. *J. Phys. Chem. A* **2011**, *115*, 3335-3345.

(39) Carr, S. A.; Glowacki, D. R.; Liang, C. H.; Baeza-Romero, M. T.; Blitz, M. A.; Pilling, M. J.; Seakins, P. W. Experimental and Modeling Studies of the Pressure and Temperature Dependences of the Kinetics and the OH Yields in the Acetyl + O_2 Reaction. *J. Phys. Chem. A* **2011**, *115*, 1069-1085.

(40) Baklanov, A. V.; Krasnoperov, L. N. Oxalyl Chloride - a Clean Source of Chlorine Atoms for Kinetic Studies. *J. Phys. Chem. A* **2001**, *105*, 97-103.

(41) Michael, J. V.; Nava, D. F.; Payne, W. A.; Stief, L. J. Rate Constants for the Reaction of Atomic Chlorine with Methanol and Dimethyl Ether from 200 - 500 K. *J. Chem. Phys.* **1979**, *70*, 3652-3656.

(42) Glowacki, D. R.; Lockhart, J.; Blitz, M. A.; Klippenstein, S. J.; Pilling, M. J.; Robertson, S. H.; Seakins, P. W. Interception of Excited Vibrational Quantum States by O_2 in Atmospheric Association Reactions. *Science (Washington, D. C., 1883-)* **2012**, *337*, 1066-1067.

(43) Lockhart, J.; Blitz, M.; Heard, D.; Seakins, P.; Shannon, R. Kinetic Study of the OH Plus Glyoxal Reaction: Experimental Evidence and Quantification of Direct OH Recycling. *J. Phys. Chem. A* **2013**, *117*, 11027-11037.

(44) Lockhart, J.; Blitz, M. A.; Heard, D. E.; Seakins, P. W.; Shannon, R. J. Mechanism of the Reaction of OH with Alkynes in the Presence of Oxygen. *J. Phys. Chem. A* **2013**, *117*, 5407-5418.

(45) Lee, T. J.; Taylor, P. R. A Diagnostic for Determining the Quality of Single-Reference Electron Correlation Methods. *Int. J. Quantum Chem.* **1989**, 199-207.

(46) MOLPRO, v., 24 a package of ab initio programs, H.-J. Werner, P. J. Knowles, G. Knizia, F. R. Manby, M. Schütz, P. Celani, T. Korona, R. Lindh, A. Mitrushenkov, G. Rauhut, K. R. Shamasundar, T. B. Adler, R. D. Amos, A. Bernhardsson, A. Berning, D. L. Cooper, M. J. O. Deegan, A. J. Dobbyn, F. Eckert, E. Goll, C. Hampel, A. Hesselmann, G. Hetzer, T. Hrenar, G. Jansen, C. Köppl, Y. Liu, A. W. Lloyd, R. A. Mata, A. J. May, S. J. McNicholas, W. Meyer, M. E. Mura, A. Nicklass, D. P. O'Neill, P. Palmieri, D. Peng, K. Pflüger, R. Pitzer, M. Reiher, T. Shiozaki, H. Stoll, A. J. Stone, R. Tarroni, T. Thorsteinsson, and M. Wang, , see http://www.molpro.net.

(47) Pilling, M. J.; Robertson, S. H. Master Equation Models for Chemical Reactions of Importance in Combustion. *Annu. Rev. Phys. Chem.* **2003**, *54*, 245-275.

(48) Blitz, M. A.; Hughes, K. J.; Pilling, M. J.; Robertson, S. H. Combined Experimental and Master Equation Investigation of the Multiwell Reaction H+SO_2. *J. Phys. Chem. A* **2006**, *110*, 2996-3009.

(49) Holbrook, K. A.; Pilling, M. J.; Robertson, S. H. *Unimolecular Reactions*, 2nd ed.; Wiley: Chichester, 1996.

(50) Klippenstein, S. J. Unimolecular Kinetics. In *Comprehensive Chemical Kinetics*; Green, N., Ed.; Elsevier: Amsterdam, 2003; Vol. 39.

(51) Davies, J. W.; Green, N. J. B.; Pilling, M. J. The Testing of Models for Unimolecular Decomposition Via Inverse Laplace Transformation of Experimental Recombination Data. *Chem. Phys. Lett.* **1986**, *126*, 373.

(52) Frisch, M. J.; Trucks, G. W.; Schlegel, H. B.; Scuseria, G. E.; Robb, M. A.; Cheeseman, J. R.; Montgomery, J. A.; Jr., T. V.; Kudin, K. N.; Burant, J. C.et al. Gaussian 03; Revision B.03 ed.; Gaussian, Inc.: Pittsburgh, 2003.

(53) Sharma, S.; Raman, S.; Green, W. H. Intramolecular Hydrogen Migration in Alkylperoxy and Hydroperoxyalkylperoxy Radicals: Accurate Treatment of Hindered Rotors. *J. Phys. Chem. A* **2010**, *114*, 5689-5701.

(54) Goldsmith, C. F.; Green, W. H.; Klippenstein, S. J. Role of O_2 + QOOH in Low-Temperature Ignition of Propane. 1. Temperature and Pressure Dependent Rate Coefficients. *J. Phys. Chem. A* **2012**, *116*, 3325-3346.

(55) Montgomery, J. A.; Frisch, M. J.; Ochterski, J. W.; Petersson, G. A. A Complete Basis Set Model Chemistry. VII. Use of the Minimum Population Localization Method. *J. Chem. Phys.* **2000**, *112*, 6532-6542.

(56) Jasper, A. W.; Miller, J. A. Collisional Energy Transfer in Unimolecular Reactions: Direct Classical Trajectories for $CH_4 = CH_3 + H$ in Helium. *J. Phys. Chem. A* **2009**, *113*, 5612-5619.

(57) Seakins, P. W.; Robertson, S. H.; Pilling, M. J.; Slagle, I. R.; Gmurczyk, G. W.; Bencsura, A.; Gutman, D.; Tsang, W. Kinetics of the Unimolecular Decomposition of Iso-C_3H_7 - Weak Collision Effects in Helium, Argon, and Nitrogen. *J. Phys. Chem.* **1993**, *97*, 4450-4458.

(58) Naik, C.; Carstensen, H.; Dean, A. M. Reaction Rate Representation Using Chebyshev Polynomials Http://Chemeng.Mines.Edu/Groups/Amdean/Public_Html/Pub/Wsspaperfinal.Pdf.

(59) Andersen, A.; Carter, E. A. Hybrid Density Functional Theory Predictions of Low-Temperature Dimethyl Ether Combustion Pathways. II. Chain-Branching Energetics and Possible Role of the Criegee Intermediate. *J. Phys. Chem. A* **2003**, *107*, 9463-9478.

(60) Curran, H. J.; Fischer, S. L.; Dryer, F. L. The Reaction Kinetics of Dimethyl Ether. II: Low-Temperature Oxidation in Flow Reactors. *Int. J. Chem. Kinet.* **2000**, *32*, 741-759.

(61) Ianni, J. C. Kintecus, Windows Version 2.80, Www.Kintecus.Com, 2002.

(62) Kurimoto, N.; Brumfield, B.; Yang, X.; Wada, T.; Dievart, P.; Wysocki, G.; Ju, Y. Quantitative Measurements of HO_2/H_2O_2 and Intermediate Species in Low and Intermediate Temperature Oxidation of Dimethyl Ether. *Proceedings of the Combustion Institute* **2014**, *In press, 10.1016/j.proci.2014.05.120*

(63) Tomlin, A. S.; Agbro, E.; Nevrly, V.; Dlabka, J.; Vasinek, M. Evaluation of Combustion Mechanisms Using Global Uncertainty and Sensitivity Analyses: A Case Study for Low Temperature DME Oxidation. *Int. J. Chem. Kinet.* **2014**, *Submitted*.

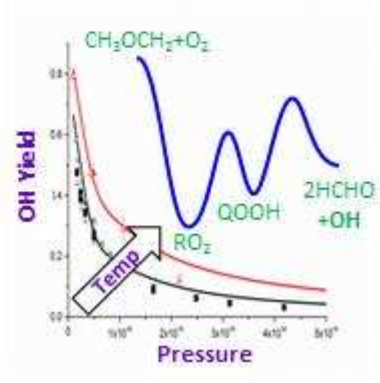

TOC picture[1]

---

[1]